Published in final edited form as:
J Clim. 2017 June 20; Volume 30(Iss 13): 5419–5454. doi:10.1175/JCLI-D-16-0758.1.

The Modern-Era Retrospective Analysis for Research and Applications, Version 2 (MERRA-2)

Ronald Gelaro[1], **Will McCarty**[1], **Max J. Suárez**[2], **Ricardo Todling**[1], **Andrea Molod**[1], **Lawrence Takacs**[3], **Cynthia Randles**[4,†], **Anton Darmenov**[1], **Michael G. Bosilovich**[1], **Rolf Reichle**[1], **Krzysztof Wargan**[3], **Lawrence Coy**[3], **Richard Cullather**[5], **Clara Draper**[2], **Santha Akella**[3], **Virginie Buchard**[2], **Austin Conaty**[3], **Arlindo da Silva**[1], **Wei Gu**[3], **Gi-Kong Kim**[1], **Randal Koster**[1], **Robert Lucchesi**[3], **Dagmar Merkova**[3,‡], **Jon Eric Nielsen**[3], **Gary Partyka**[3], **Steven Pawson**[1], **William Putman**[1], **Michele Rienecker**[1], **Siegfried D. Schubert**[1], **Meta Sienkiewicz**[3], **Bin Zhao**[6]

[1]Global Modeling and Assimilation Office, NASA Goddard Space Flight Center, Greenbelt, MD

[2]Universities Space Research Association, Columbia, MD

[3]Science Systems and Applications, Inc., Lanham, MD

[4]Morgan State University, Baltimore, MD

[5]Earth System Science Interdisciplinary Center, College Park, MD

[6]Science Applications International Corporation, Beltsville, MD

Abstract

The Modern-Era Retrospective Analysis for Research and Applications, Version 2 (MERRA-2) is the latest atmospheric reanalysis of the modern satellite era produced by NASA's Global Modeling and Assimilation Office (GMAO). MERRA-2 assimilates observation types not available to its predecessor, MERRA, and includes updates to the Goddard Earth Observing System (GEOS) model and analysis scheme so as to provide a viable ongoing climate analysis beyond MERRA's terminus. While addressing known limitations of MERRA, MERRA-2 is also intended to be a development milestone for a future integrated Earth system analysis (IESA) currently under development at GMAO. This paper provides an overview of the MERRA-2 system and various performance metrics. Among the advances in MERRA-2 relevant to IESA are the assimilation of aerosol observations, several improvements to the representation of the stratosphere including ozone, and improved representations of cryospheric processes. Other improvements in the quality of MERRA-2 compared with MERRA include the reduction of some spurious trends and jumps related to changes in the observing system, and reduced biases and imbalances in aspects of the water cycle. Remaining deficiencies are also identified. Production of MERRA-2 began in June 2014 in four processing streams, and converged to a single near-real time stream in mid 2015. MERRA-2 products are accessible online through the NASA Goddard Earth Sciences Data Information Services Center (GES DISC).

Corresponding author: Ronald Gelaro, Global Modeling and Assimilation Office, NASA Goddard Space Flight Center, Greenbelt, MD 20771, USA. ron.gelaro@nasa.gov.
†Current affiliation: ExxonMobil Corporate Strategic Research, Annandale, NJ
‡Current affiliation: I.M. System Group, Inc., Rockville, MD

1. Introduction

Reanalysis is the process whereby an unchanging data assimilation system is used to provide a consistent reprocessing of meteorological observations, typically spanning an extended segment of the historical data record. The process relies on an underlying forecast model to combine disparate observations in a physically consistent manner, enabling production of gridded data sets for a broad range of variables including ones that are sparsely or not directly observed. As such, and with appropriate consideration of the inherent uncertainties, reanalysis products have not only become a staple of the atmospheric research community, but are used increasingly for climate monitoring as well as for business applications in, for example, energy and agriculture. Recent reanalyses from the National Oceanic and Atmospheric Administration/National Centers for Environmental Prediction (NOAA/NCEP), the European Centre for Medium-Range Weather Forecasts (ECMWF), the National Aeronautics and Space Administration/Global Modeling and Assimilation Office (NASA/GMAO), and the Japan Meteorological Agency (JMA) provide a rich ensemble of climate data products beginning more or less with the period of regular conventional and satellite observations in the mid to late twentieth century (Saha et al. 2010; Dee et al. 2011; Rienecker et al. 2011; Kobayashi et al. 2015). However, there have also been successful efforts to extend atmospheric reanalyses back to the late nineteenth and early twentieth centuries using only surface pressure observations (Compo et al. 2011) or surface and mean sea level pressure observations plus surface marine winds (Poli et al. 2013). As noted by Dee et al. (2011), these century-long reanalyses have also sparked remarkable data recovery and digitization efforts by various groups around the world.

The GMAO's reanalysis development effort began (under its predecessor organization, the Data Assimilation Office) with the production of the Goddard Earth Observing System, version 1 (GEOS-1) reanalysis (Schubert et al. 1993), but advanced significantly with the more recent production of the Modern-Era Retrospective Analysis for Research and Applications (MERRA, Rienecker et al. 2011). MERRA encompassed the period 1979–2016 and was undertaken with two primary objectives: to place NASA's Earth Observing System (EOS) satellite observations in a climate context and to improve the representation of the atmospheric branch of the hydrological cycle compared with previous reanalyses. MERRA succeeded in meeting these objectives overall and was found to be of comparable quality to contemporaneous reanalyses produced by NCEP and ECMWF (e.g., Decker et al. 2011). However, it also suffered from a number of known, but not necessarily unique, deficiencies. These include unphysical jumps and trends in precipitation in response to changes in the observing system, biases and imbalances in certain atmospheric and land surface hydrological quantities, and a poor representation of the upper stratosphere (e.g., Bosilovich et al. 2011; Robertson et al. 2011; Reichle et al. 2011; Rienecker et al. 2011). In addition, the long-term viability of MERRA was limited by system constraints that precluded the incorporation of new satellite data sources beyond NOAA-18, which launched in 2005. At the time of its termination in March 2016, MERRA was at risk of suffering a significant degradation in quality were certain observing platforms to fail, including, for example, EOS Aqua, which was already well beyond its designed lifetime and provided

MERRA with its only sources of hyperspectral infrared and afternoon-orbit microwave radiances.

The Modern Era Retrospective Analysis for Research and Applications, version 2 (MERRA-2) was undertaken to provide a timely replacement for MERRA and to sustain GMAO's commitment to having an ongoing near-real-time climate analysis. MERRA-2 is intended as an intermediate reanalysis; one that leverages recent developments at GMAO in modeling and data assimilation to address some of the known limitations of MERRA, but also provides a stepping stone to GMAO's longer term goal of developing an integrated Earth system analysis (IESA) capability that couples assimilation systems for the atmosphere, ocean, land and chemistry. Toward the latter goal MERRA-2 includes aerosol data assimilation, thereby providing a multi-decadal reanalysis in which aerosol and meteorological observations are jointly assimilated within a global data assimilation system. Other new developments in MERRA-2 relevant to IESA focus on aspects of the cryosphere and stratosphere, including the representation of ozone, and on the use of precipitation observations to force the land surface. At the same time, basic aspects of the MERRA-2 system, such as the variational analysis algorithm and observation handling, are largely unchanged since MERRA. Also unchanged is the preparation of most conventional data sources used originally in MERRA.

This paper presents an overview of MERRA-2, including a description of the data assimilation system and various measures of performance. Some of these measures focus on difficulties encountered in MERRA while others highlight new capabilities such as the assimilation of aerosol observations. This paper also serves as an introduction to a series of companion papers that provide more detailed analyses of the topics covered in this overview as well as others. For example, a detailed description of the MERRA-2 aerosol analysis system and its validation are presented in Randles et al. (2017) and Buchard et al. (2017). Reichle et al. (2017a,b) assess the land surface precipitation and land surface hydrology, while Draper et al. (2017) examine the land surface energy budget. Bosilovich et al. (2017) evaluate the global water balance and water cycle variability in MERRA-2. Collow et al. (2016) examine MERRA-2's representation of US summertime extreme precipitation events, and Lim et al. (2017) investigate aspects of major El Nino events. Collow and Miller (2016) examine the radiation budget and cloud radiative effect over the Amazon. Segal-Rosenhemier et al. (2017) examine surface radiative fluxes in polar marginal ice zones. Several papers investigate aspects of the stratosphere in MERRA-2: Wargan et al. (2017) examine the representation of lower stratospheric ozone and the effect of assimilating ozone observations from NASA's Aura satellite; Coy et al. (2016) examine the representation of the quasi-biennial oscillation in MERRA-2; and Wargan and Coy (2016) present a case study of the 2009 sudden stratospheric warming.

Section 2 provides an overview of the MERRA-2 data assimilation system, focusing primarily on developments since MERRA, including new observation sources. Basic metrics of the assimilation system performance are presented in section 3. The MERRA-2 aerosol analysis is described in section 4, along with sample results and validation statistics. Section 5 examines global and regional aspects of the representation of precipitation in MERRA-2, focusing on areas of difficulty in MERRA. Stratospheric processes and the representation of

ozone are discussed in section 6. Section 7 addresses the representation of the cryosphere in MERRA-2, with focus on glaciated land surface processes. Section 8 provides information about MERRA-2 products and how they can be accessed. It is noted here that each MERRA-2 data collection has its own digital object identifier (DOI) number, so data used in scientific publications can be cited exactly. Most of the results shown for MERRA-2 in this paper are derived from these collections, which are individually cited in the corresponding figure captions. Finally, a brief summary and perspective on future work are presented in section 9. A list of acronyms is given in the Appendix.

2. MERRA-2 system description

MERRA-2 is produced with version 5.12.4 of the Goddard Earth Observing System (GEOS-5.12.4) atmospheric data assimilation system. The key components of the system are the GEOS atmospheric model (Rienecker et al. 2008; Molod et al. 2015) and the Gridpoint Statistical Interpolation (GSI) analysis scheme (Wu et al. 2002; Kleist et al. 2009b). The model includes the finite-volume dynamical core of Putman and Lin (2007), which uses a cubed sphere horizontal discretization at an approximate resolution of 0.5° × 0.625° and 72 hybrid-eta levels from the surface to 0.01 hPa. The analysis is computed on a latitude-longitude grid at the same spatial resolution as the atmospheric model using a three-dimensional variational (3DVAR) algorithm based on the GSI with a 6-h update cycle and the so-called first-guess-at-appropriate-time (FGAT) procedure for computing temporally accurate observation-minus-background departures. The analysis is applied as a correction to the background state using an incremental analysis update (IAU) procedure (Bloom et al. 1996).

The MERRA-2 system has many of the same basic features as the MERRA system (GEOS-5.2.0) described in Rienecker et al. (2011) but includes a number of important updates. An overview of these updates is provided here, with additional details provided in companion publications as cited. Unless otherwise stated, other aspects of the system configuration and preparation of the input data are as described in Rienecker et al. (2011). The updates discussed here include changes to the forecast model (section 2a), the analysis algorithm (section 2b), the observing system (section 2c), the radiance assimilation (section 2d), the bias correction of aircraft observations (section 2e), the mass conservation and water balance (section 2f), the precipitation used to force the land surface and drive wet aerosol deposition (section 2g), the boundary conditions for sea surface temperature and sea ice concentration (section 2h), and reanalysis production (section 2i).

a. Forecast model

Since MERRA, the GEOS model has undergone changes to both its dynamical core and its physical parameterizations. Whereas in MERRA the horizontal discretization of the model was computed on a latitude-longitude grid, MERRA-2 uses a cubed sphere grid. This allows relatively uniform grid spacing at all latitudes and mitigates the more severe grid spacing singularities that occur on a latitude-longitude grid. Upgrades to the physical parameterization schemes include increased re-evaporation of frozen precipitation and cloud condensate, changes to the background gravity wave drag, and an improved relationship

between the ocean surface roughness and ocean surface stress (Molod et al. 2015). The MERRA-2 model also includes a Tokioka-type trigger on deep convection as part of the Relaxed Arakawa-Schubert (RAS, Moorthi and Suárez 1992) convective parameterization scheme, which governs the lower limit on the allowable entrainment plumes (Bacmeister and Stephens 2011). A new glaciated land representation and seasonally-varying sea ice albedo have been implemented, leading to improved air temperatures and reduced biases in the net energy flux over these surfaces (Cullather et al. 2014).

b. Analysis algorithm

The control variable for moisture used in recent versions of GSI and MERRA-2 differs from the one used in MERRA. Whereas MERRA used the so-called pseudo-relative humidity (Dee and da Silva, 2003) defined by the water vapor mixing ratio scaled by its saturation value, MERRA-2 uses the normalized pseudo-relative humidity (Holm 2003) defined by the pseudo-relative humidity scaled by its background error standard deviation. The latter has a near Gaussian error distribution, making it more suitable for the minimization procedure employed in the assimilation scheme. Also within the GSI, a tangent linear normal mode constraint (TLNMC, Kleist et al. 2009a) is applied during the minimization procedure to control noise and improve the overall use of observations. The background error statistics used in the GSI have been updated as well in MERRA-2. As in MERRA, the statistics are estimated using the ‘NMC’ method (Parrish and Derber, 1992) by calculating variances and covariances from the differences between 24-h and 48-h forecasts, but from a more recent version of GEOS. Compared with the MERRA system, the background error statistics for the MERRA-2 system exhibit generally smaller standard deviations for most variables, but both larger and smaller correlation length scales depending on the variable, latitude and vertical level.

c. Observing system

MERRA included no new satellite observation sources after the introduction of NOAA-18 in 2005. MERRA-2, in contrast, includes numerous additional satellite observations both before and after this time. The complete set of input observations assimilated in MERRA-2 is summarized in Table 1, while a detailed description of their use is provided in McCarty et al. (2016). Additions to the MERRA-2 observing system compared with MERRA include:

- Atmospheric motion vectors from the Advanced Very High Resolution Radiometer (AVHRR);
- Surface wind speeds from the Special Sensor Microwave Imager/Sounder (SSMIS);
- Surface wind vectors from the Meteorological Operational Satellite-A (Metop-A) Advanced Scatterometer (ASCAT) and WindSat;
- Temperature and ozone profiles from the EOS Aura Microwave Limb Sounder (MLS);
- Total column ozone from the EOS Aura Ozone Monitoring Instrument (OMI);
- Bending angle from Global Positioning System radio occultations (GPSRO);

- Microwave and infrared sounding radiances from the Advanced TIROS Operational Vertical Sounder (ATOVS) on NOAA-19, Metop-A and -B;
- Microwave sounding radiances from the Advanced Technology Microwave Sounder (ATMS) on the Suomi National Polar-orbiting Partnership (SNPP);
- Hyperspectral infrared radiances from the Infrared Atmospheric Sounding Interferometer (IASI) on Metop-A and -B, and from the Cross-track Infrared Sounder (CrIS) on SNPP;
- Geostationary radiances from the Meteosat Second Generation (MSG) Spinning Enhanced Visible Infrared Imager (SEVIRI) and Geostationary Operational Environmental Satellites (GOES-11, −13 and −15).

Time series of the various types of observations assimilated in MERRA and MERRA-2 are shown in Figure 1. The number of assimilated observations in MERRA-2 grows from approximately two million per 6-h cycle in 2002 to almost five million in 2015, while MERRA assimilates approximately 1.5 million observations per 6-h cycle from 2002 onward. The GSI in MERRA-2 is also capable of assimilating microwave and hyperspectral infrared radiances from planned future satellites including Metop-C and the Joint Polar Satellite System (JPSS). The temporary spike in the number of QuikSCAT data assimilated in MERRA-2 in late 2000 is due to an error in preprocessing which led to observations beyond the mid-swath “sweet spot” being used in the analysis. This has no discernible impact on the quality of the analyzed fields or on the use of other observations in the assimilation system.

MERRA-2 also assimilates reprocessed versions of some of the same satellite observation types used in MERRA. In MERRA-2, Remote Sensing Systems version 7 (RSS v7) recalibrated radiances and retrieved surface wind speeds from the Defense Meteorological Satellite Program (DMSP) Special Sensor Microwave Imager (SSM/I) are used, whereas MERRA used RSS v6. The use of retrieved ozone from the Solar Backscatter Ultraviolet Radiometer (SBUV) also differs, with MERRA-2 assimilating version 8.6 on 21 layers from 1980 thru 2004 before switching to OMI and MLS in October 2004. In contrast, MERRA used SBUV version 8 throughout, in a form degraded from its original 21 layers to 12.

d. Radiance assimilation

Radiative transfer calculations necessary for the assimilation of satellite radiances in MERRA-2 are performed using the Community Radiative Transfer Model (CRTM, Han et al. 2006, Chen et al. 2008). MERRA-2 uses version 2.1.3 of the CRTM for assimilation of all satellite radiances, whereas MERRA used a prototype version of the CRTM for all radiances except those from the Stratospheric Sounding Unit (SSU), for which the Goddard Laboratory for Atmospheres TOVS forward model (GLATOVS, Susskind et al. 1983) was used. Differences between the prototype and version 2.1.3 of the CRTM are too numerous to mention here, but a detailed description of the latter can be found in Liu and Boukabara (2014).

The actively assimilated channels for each satellite sensor type in MERRA-2 are summarized in Table 2. Microwave temperature sounding channels with strong surface

sensitivity—so-called window channels—are not assimilated in MERRA-2, in part because of the strong sensitivity of global precipitation and humidity to these data found in MERRA (Robertson et al. 2011). These include channels 1–3 and 15 on the Advanced Microwave Sounding Unit-A (AMSU-A), channels 1–4 and 16 on ATMS, and channel 1 on the Microwave Sounding Unit (MSU). For microwave humidity sounders including the the Advanced Microwave Sounding Unit-B (AMSU-B) and Microwave Humidity Sounder (MHS), window channels are actively assimilated along with the sounding channels. For heritage infrared sounders, channels 13–15 on the High-resolution Infrared Radiation Sounder (HIRS) were assimilated in MERRA but are excluded in MERRA-2. The channel selections for hyper-spectral infrared sounders and performance assessments for selected instruments are provided in McCarty et al. (2016).

Like MERRA, MERRA-2 uses an automated bias correction scheme for the assimilation of most satellite radiance observations. Bias estimates for individual sensor channels are represented by a small number of predictors which can depend on the atmospheric state, the radiative transfer model, and the sensor characteristics. Air-mass- and viewing angle-dependent biases are estimated using a variational scheme in which the predictor coefficients are updated as part of the control vector used to minimize the analysis cost function (Derber and Wu, 1998). Satellite scan-position-dependent bias is estimated directly as an exponential moving average filter of the observation-minus-background departures for brightness temperature. For both the variational and scan-position predictors, initial values of the coefficients for MERRA-2 were derived from GEOS operations and other long production runs using system versions similar to that used for MERRA-2. In the few cases where no recent coefficient information was available, initial values were derived from MERRA. Note that no bias correction is applied to a small number of sensor channels that peak in the upper stratosphere, including channel 14 on AMSU-A, channel 15 on ATMS, and channel 3 on SSU. This is done to prevent the variational bias correction scheme—which is formulated to remove systematic discrepancies between the observations and the background state irrespective of the source—from making erroneous adjustments to the observations at levels where model biases are known to be large.

e. Bias correction of aircraft temperature observations

A bias correction scheme for aircraft temperature observations has been implemented in MERRA-2, motivated by the known warm bias of these measurements compared with other data sources (Cardinali et al. 2003, Ballish and Kumar 2008; Rienecker et al. 2011). The scheme uses the mean observed-minus-background departures to estimate the bias for temperature reports from individual aircraft, identified by their tail number. The bias estimates are updated after each analysis. The scheme is used to correct Aircraft Meteorological Data Relay (AMDAR) and Aircraft Communications Addressing and Reporting (ACARS) reports only, since other sources of aircraft observations in MERRA-2 do not have unique identifiers by which they can be tracked. As of 2015, bias corrections for approximately 3700 separate aircraft are tracked in MERRA-2.

The performance of the scheme is discussed in McCarty et al (2016). As expected, the scheme is shown to reduce the bias between the corrected aircraft observations and the

background forecast, as well as reduce the variance of the corrected background departures, allowing more aircraft observations to be used in the analysis. Unfortunately, the MERRA-2 background state was found to have a larger than expected positive bias in the mid- to upper troposphere, which feeds back to the bias estimates. The result is that the bias correction actually increases the aircraft temperatures in some cases, and the fit to other unbiased observation types such as radiosondes is degraded. This is discussed further in section 3.

f. Mass conservation and water balance

Studies have documented the difficulty of maintaining realistic balances between variations in total mass and total water content in previous reanalyses (e.g., Trenberth and Smith 2005; Bosilovich et al. 2011; Berrisford et al. 2011). These studies show that analysis adjustments to moisture are often large (when, ideally, they should be small), highly sensitive to changes in the observing system, and mostly balanced by unphysical changes in precipitation. Takacs et al. (2016) argue that, in attempting to analyze the total mass of the atmosphere from surface pressure observations, reanalyses may violate the simple physical constraint that, to an excellent approximation, the total dry mass of the atmosphere is invariant, and so changes in total mass must be essentially equivalent to changes in total water mass. At the same time, Berrisford et al. (2011) argue that, while the observing system may not provide the data to determine exactly the total mass of the atmosphere, the degree to which dry mass is preserved in a reanalysis provides a useful diagnostic of reanalysis quality.

Reconsideration of these issues during the development of MERRA-2 prompted modifications to GEOS to conserve atmospheric dry mass and to guarantee that the net source of water from precipitation and surface evaporation equals the change in total atmospheric water. As described by Takacs et al. (2016), this has been achieved by making the following changes to the forecast model and assimilation procedure:

- Sources and sinks of atmospheric water have been added to the model continuity equation so that changes in total mass are driven purely by changes in total water.
- A constraint that penalizes analysis increments of dry air has been added to the GSI.
- Tendencies in the IAU are rescaled so that the global mean is removed from the analysis increment of water.

The global impact of these modifications is illustrated in Figures 2 and 3, which compare different components of atmospheric mass in MERRA and MERRA-2. Figure 2 shows monthly mean anomalies from the mean seasonal cycle for total mass, total water, and dry-air mass in the two reanalyses. In MERRA, there is an increase in total water over the period, with significant inter-annual variations, but these features do not necessarily match the changes in total mass. There also are spurious anomalies in dry-air mass throughout, some of which track closely with the changes in total mass. In MERRA-2, changes in total mass and total water track each other almost perfectly, by design, and the dry-air mass remains a constant whose value must be specified. For the latter, the value 983.24 hPa is chosen based on MERRA. This value falls within 0.1% of the values derived from other recent reanalyses (Takacs et al. 2016).

Figure 3 shows monthly mean values of evaporation minus precipitation ($E - P$, or water source term), the vertically integrated analysis increment of water, and the atmospheric water storage. Note that the atmospheric water storage has similar magnitude in both reanalyses and is dominated by the seasonal cycle. In MERRA, however, the storage is determined by a near balance between the large and highly variable contributions from the analysis increment on the one hand, and unphysical variations in $E - P$ of the opposite sign on the other hand. This includes an abrupt change in the sign of these quantities after the introduction of AMSU-A in 1998 (Robertson et al. 2011). In MERRA-2, the globally integrated analysis increment is zero, by design, and the water storage is determined as in nature by small seasonal differences in E and P. It should be noted that removing the global mean analysis increments of total mass and water mass does not imply that the analysis increments of water vapor or surface pressure vanish locally, as shown in Section 3 of this paper and discussed in further detail by Bosilovich et al. (2017).

g. Observation-corrected precipitation forcing

The precipitation generated by the atmospheric model during the IAU segment of the assimilation procedure is subject to considerable errors that can propagate into land surface hydrological fields and beyond (Reichle et al. 2011). To mitigate these effects in MERRA-2, the model-generated precipitation is corrected with observations before being used to force the land surface or affect the wet deposition of aerosols over land and ocean. Both the model-generated precipitation and the precipitation seen by the land surface and the aerosols are available in the MERRA-2 output. MERRA-2 is one of several recent applications of GEOS that uses observation-corrected precipitation estimates. Others include the GMAO seasonal forecasting system (Ham et al. 2014), the MERRA-Land data product (Reichle et al. 2011), and the MERRAero aerosol reanalysis (Buchard et al. 2015). Precipitation observations have also been used in reanalyses produced by NOAA, including the North American Regional Reanalyis (Mesinger et al. 2006) and in the Climate Forecast System Reanalysis (CFSR, Saha et al. 2010; Meng et al. 2012), although in both cases the approaches differ from that used in MERRA-2. Some discussion of the differences between the approaches used in MERRA-2 and CFSR can be found in Reichle et al. (2017a).

The corrected precipitation in MERRA-2 is derived from publicly available, observationally based global precipitation products disaggregated from daily or pentad totals to hourly accumulations using precipitation estimates from MERRA (Reichle and Liu 2014; Reichle et al. 2017a). The land surface in MERRA-2 sees a combination of corrected and model-generated precipitation depending on latitude, with the land surface forced primarily by the corrected estimates at low to mid-latitudes, by the MERRA-2 model-generated precipitation at high latitudes, and by a weighted mixture in between to prevent spatial discontinuities in climatological means. This is illustrated in Figure 4, which shows the annual average adjustment made to the model-generated precipitation in MERRA-2 for the period 1980–2015 using this technique. The greatest adjustments are made in the tropics, where precipitation is greatest and the corrected estimates are given most weight, while no adjustments are made poleward of 62.5° in either hemisphere.

Based on the evaluation of several metrics, Reichle et al. (2017a) found the observation-corrected precipitation to be more realistic overall than that generated by the model within the cycling MERRA-2 system, or that of the MERRA and MERRA-Land data products. Exceptions include discontinuities in the MERRA-2 corrected precipitation that result from errors in the underlying gauge products, for example, in Myanmar and South America. Another issue is the high bias in MERRA-2 summer precipitation in the high latitudes (where precipitation observations are not used). Moreover, the diurnal cycle of the MERRA-2 corrected precipitation has reasonable amplitudes compared to independent observations, but the time-of-day of maximum precipitation is inherited from MERRA and is unrealistic.

The improvements in the precipitation forcing are also reflected in the MERRA-2 land surface estimates. Reichle et al. (2017b) show that soil moisture, snow, terrestrial water storage, and runoff in MERRA-2 agree better with independent observations than estimates from MERRA. Draper et al. (2017) further demonstrate that the temporal behavior and long term mean values of the land-atmosphere turbulent fluxes in MERRA- 2 are improved. Moreover, by applying the precipitation corrections within the coupled atmosphere-land modeling system, MERRA-2 can provide more self-consistent surface meteorological data than were used for MERRA-Land (Reichle et al. 2017a). This self-consistency is important for applications such as forcing land-only model simulations.

Finally, it should be noted that the atmospheric water and energy prognostic variables associated with the creation of precipitation in MERRA-2 are not directly modified by the corrected estimates, although they can be indirectly modified through subsequent feedback with the land surface.

h. Sea surface temperature and sea ice concentration

The boundary conditions for sea surface temperature (SST) and sea ice concentration (SIC) in MERRA were based on the 1° weekly (or monthly) product of Reynolds et al. (2002). In MERRA-2, SST and SIC boundary conditions are instead based on currently available high-resolution (finer than 1°) daily products. However, as there exists no continuous source of daily global high-resolution SST and SIC for the entire period of MERRA-2—and no source of daily data whatsoever prior to 1982—the following products were used in combination (Table 3): monthly 1° data from the Coupled Model Intercomparison Project (CMIP) as in Taylor et al. (2000) for the period prior to 1982; daily 1/4° data from the NOAA Optimum Interpolation Sea Surface Temperature (OISST) as in Reynolds et al. (2007) from 1982 thru March 2006; and daily 1/20° data from the Operational Sea Surface Temperature and Sea Ice Analysis (OSTIA) as in Donlon et al. (2012) from April 2006 onwards. Note that different versions of the NOAA OISST product are used prior to and after January 2003, the latter including satellite data from both AVHRR and the Advanced Microwave Scanning Radiometer-EOS (AMSR-E) on NASA’s Aqua satellite, and the former including satellite data from AVHRR only. The processing of these products into a unified gridded set of daily SST and SIC boundary conditions for MERRA-2 is described in Bosilovich et al. (2015). Care was taken to use both SST and SIC from the same data source to avoid potential inconsistencies, especially in marginal ice zones.

Figure 5 shows 12-month running averaged values of SST between 60°N and 60°S for MERRA-2 and several other reanalyses, including MERRA. In all cases, there is a positive trend in SST throughout the period. The running means for all the reanalyses are within 1 K for the 30 years spanning 1980–2010, and the anomalies (not shown) are separated by less than 0.2 K. At the same time, there are clear systematic differences between reanalyses, with the MERRA-2 SST's on the one hand being cooler than those used in the other reanalyses shown except CFSR (which used similar input data sets), especially before the transition to OSTIA in 2006. The values for JRA-55, on the other hand, are on the order of 0.1 K higher than other reanalyses throughout the 35-year period. It can also be seen that the MERRA-2 SSTs increase slightly with the change in NOAA OISST versions after 2003. The reader is referred to Bosilovich et al. (2015) for a more detailed list of known issues with the SST and SIC boundary conditions for MERRA-2.

i. Production

MERRA-2 was produced in four separate streams, each of which was spun up for a year at full resolution beginning on 1 January 1979 (stream 1), 1 January 1991 (stream 2), 1 January 2000 (stream 3) and 1 January 2010 (stream 4). The land surface restart files for each MERRA-2 stream were themselves spun up for at least 20 years using the off-line MERRA-2 land model forced by MERRA surface meteorological fields, and with the precipitation replaced by the observation-corrected estimates described in section 2g. The final MERRA-2 product distribution is from stream 1 for 1 January 1980–31 December 1991, followed by stream 2 for 1 January 1992–31 December 2000, then stream 3 for 1 January 2001–31 December 2010, and finally stream 4 for 1 January 2011-present. With streams 1–3 complete, MERRA-2 production continues as a near-real time climate analysis from stream 4 alone. The decision to begin stream 1 in January 1979 and distribute products beginning in January 1980—a year later than the schedule followed in MERRA—was based on the fact that the products used to create the observation-corrected precipitation estimates for MERRA-2 only start on 1 January 1979, leaving no viable way to initialize the land surface properly before this time (which requires several months of spin-up, after initialization from climatological conditions).

The overlap periods between successive streams were examined to determine the adequacy of the spin-up procedure and to quantify the uncertainty in individual fields. Differences between overlapping MERRA-2 streams were found to be minimal for most fields after one year, with the exception of certain land surface variables including the deep-level soil temperature and land surface soil moisture storage at high latitudes. The spin-up of the land surface is addressed separately in Reichle et al. (2017a); section 3d and Figure 13 of that paper discuss specific examples of the aforementioned discontinuities across consecutive MERRA-2 streams. Users should be aware of these discontinuities when the data are used for specific applications.

3. Data assimilation diagnostics

By-products of the data assimilation procedure in the form of differences between forecasts and observations, analysis increments, and estimates of bias can be used effectively to

monitor the quality of both the input and output of the assimilation. In this section, examples of such diagnostics are presented for MERRA-2, focused mainly on feedbacks with respect to in-situ conventional observations and on the net correction, or increment, brought by the entirety of the assimilated observations. The reader is referred to McCarty et al. (2016) for examples of feedbacks related to the treatment of satellite radiance observations.

a. Background departure statistics

Differences between the assimilated observations and the background forecast, referred to as innovations or background departures, provide important information about the quality of the assimilation. In particular, it is important that the assimilation system be able to predict high-quality observations, especially for conventional data types which provide direct measurements of the analyzed variables. In addition to affecting the analysis directly, many conventional data play an important role in anchoring the variational bias estimates used in the assimilation of satellite radiances. Generally speaking, smaller background departures indicate a higher quality assimilation. The results shown here are selected to highlight both strengths and weaknesses of MERRA-2 in this regard. As in MERRA, for convenience, gridded versions of the observations and corresponding departures used in MERRA-2 will be made available to users.

Figure 6 shows time series of monthly mean and root mean square (RMS) background departure statistics for all assimilated surface pressure observations in MERRA and MERRA-2 for both the Northern and Southern Hemisphere. Also shown are the monthly mean numbers of surface pressure observations assimilated in each 6-h assimilation cycle in MERRA-2. The RMS values decrease with time in both reanalyses, especially in the Southern Hemisphere after the early to mid 1990's when the number of observations begins to increase significantly. The RMS values in the Northern Hemisphere (Figure 6a) are smaller than in the Southern Hemisphere initially and decrease more slowly with time, reflecting the greater number of conventional observations available over land throughout the period. This decrease is slightly more pronounced in MERRA-2 after the mid 1990's when the number of surfaces pressure observations from land stations increases significantly. In the Southern Hemisphere (Figure 6b), the RMS values are larger in MERRA-2 than in MERRA before the mid 1990's but smaller by the end of the period. The larger values early on are due to the use of larger observation errors for surface ship observations (and some other conventional data types) in MERRA-2, allowing more "outliers" with larger departure values to pass the quality control procedure in the analysis.[1] The impact diminishes by the mid 1990's as other observation types, including from satellites, become more abundant. There is no similar effect in the Northern Hemisphere where surface pressure observations from land stations are dominant early in the period; the observation errors specified for these data are the same in MERRA and MERRA-2. Finally, the jump in RMS values in the Southern Hemisphere evident in both reanalyses at the beginning of 1985 coincides with the introduction of regularly spaced synthetic surface pressure observations over southern ocean areas.

[1]The observation errors for conventional data types have been adjusted since MERRA-2.

The mean background departures for surface pressure in the Northern Hemisphere are consistently less biased in MERRA-2 than in MERRA, especially after the mid 1990's. In the Southern Hemisphere, however, the departures for MERRA-2 show a negative bias throughout the period; this is discussed further in section 3b. The mean departures in MERRA-2 also show a more pronounced annual cycle in this hemisphere. As a point of reference, the background departure statistics for other reanalyses including, for example, ERA-Interim (Dee at al. 2011) exhibit a clear annual cycle, but with somewhat smaller amplitude than in MERRA-2.

Figure 7 shows global background departure statistics for radiosonde temperatures for MERRA and MERRA-2 at selected pressure levels in the troposphere (300 hPa and 700 hPa) and stratosphere (10 hPa and 50 hPa). Also shown for each level are the monthly mean numbers of radiosonde temperature observations assimilated in each 6-h assimilation cycle in MERRA-2. In the troposphere (Figures 7c and d), the performance of MERRA-2 is degraded compared to that of MERRA, especially at 300 hPa. The RMS values for MERRA-2 decrease with time but remain 10–20% larger than those for MERRA during much of the period. Again, this is due at least partially to the use of larger observation errors for radiosonde temperatures and other conventional data types in MERRA-2. Noticeable improvements occur first in the mid 1990's when satellite observations become more abundant, and again in 2006 when the number of GPSRO observations increases significantly.

The mean departure values at 300 hPa for both MERRA and MERRA-2 exhibit a clear negative bias. The bias is generally larger in MERRA-2, reaching a maximum amplitude of greater than 0.5 K during the early 2000's. This is due to a warm model bias in the upper troposphere which worsened during the course of development between MERRA and MERRA-2 (see also Figure 10). However, aspects of the assimilation process may exacerbate the problem. It can be seen for example that the bias in the background departures at 300 hPa increases noticeably after the mid 1990's, especially in MERRA-2, when the numbers of both aircraft temperature observations and satellite radiances begin to increase significantly (Figure 1). The design of the bias correction procedures for both observation types is such that they result in an adjustment of the observations regardless of the source of the bias. In the presence of a strong model bias this can reinforce the actual observational bias and cause the assimilation system to drift further toward the model state, as noted in the case of the aircraft bias corrections described in section 2e. A similar, though less direct, effect may occur through the observational bias corrections used to assimilate satellite radiances, although other aspects of the variational scheme used to adjust these data act to reduce this risk (Dee and Uppala 2009). At 700 hPa, the mean departures for both reanalyses are generally more comparable and considerably less biased.

In the stratosphere (Figures 7a and b), there are fewer significant differences between the results for MERRA and MERRA-2 although the departures at 10 hPa for MERRA-2 show a larger negative bias of −0.2 K to −0.3 K prior to the early 2000's. After 2002, when assimilation of AIRS radiances begins, the biases at 10 hPa in both reanalyses exhibit an upward trend and eventually become positive, first in MERRA around 2003 and then in MERRA-2 in 2005. There is a discernible jump in the mean departures at this level for

MERRA-2 in 2005. This is around the time when assimilation of both MLS temperature retrievals (above 5 hPa) and GPSRO bending angle observations (up to approximately 10 hPa) begins in MERRA-2, but this does not appear to improve the fit to radiosondes at 10 hPa compared with MERRA. After 2006, the biases in both reanalyses have average values of 0.2 K to 0.3 K. Finally, at 50 hPa, the departure values for both reanalyses are very similar and exhibit only a small positive bias throughout.

Figure 8 shows statistics for radiosonde specific humidity background departures at 500 and 850 hPa in the tropics. The performance of MERRA-2 is slightly worse than that of MERRA in the middle troposphere in terms of both RMS and bias, but similar or slightly better in the lower troposphere. Again, the mean departure values are consistent with known biases in the GEOS model.

b. Analysis increments

The analysis increments represent the net adjustment to the background state by the assimilation scheme in response to all the observations. As this adjustment depends in a complex way on assumed or crudely estimated errors in the observations and background state, and on the forward operator that transforms the model variables to observation space, the increments do not necessarily represent errors in the background state. Nonetheless, their spatial and temporal variations provide an important diagnostic of system performance, including how changes in the observing system may affect the consistency of the analysis. Systematic increments often indicate the presence of biases in the model or observations which may complicate the use of reanalyses for estimating budgets and identifying trends (Dee et al. 2011).

As described in section 2, the GEOS assimilation system uses an IAU procedure which, instead of correcting the initial condition, applies the analysis increment to the model as a constant tendency term during the 6-h assimilation window. It is this contribution to the time tendency from the analysis that is provided as a standard output quantity in MERRA-2, examples of which are presented here. For convenience, these are referred to as simply the analysis increments in the discussion that follows.

Figure 9 shows the mean and standard deviation in time of the monthly mean analysis increment of surface pressure in MERRA-2 for the period January 1980 through December 2015. The monthly means themselves have been computed from sub-daily data, eight times per day. The pattern of the mean increments indicates that the analysis tends to move mass from the oceans to the continents, as noted also by Takacs et al. (2016), although this pattern is arguably most robust in the Southern Hemisphere. (The mostly negative surface pressure increments over Canada provide an obvious counter example.) These results are consistent with those in Figure 6 showing a negative bias in the Southern Hemisphere background departures in MERRA-2. The standard deviation of the increments shows that the largest variations in surface pressure occur in the middle and high latitudes, and especially over coastal Antarctica and the mountainous regions of southern and eastern Asia, as well as southern Alaska.

Time series of the global monthly mean and standard deviation of the analysis increments of temperature from the surface to 70 hPa in MERRA-2 are shown in Figure 10. The most striking feature in the mean increments is the persistent cooling by the analysis in the layer between 250 and 400 hPa. This is consistent with the negative bias in the background departures at 300 hPa shown in Figure 7 and provides further evidence of the warm model bias at these levels. Except for seasonal variations, the magnitude of the cooling remains relatively constant throughout much of the period, although noticeable changes occur, for example, beginning in the mid to late 1990's as the number of aircraft and satellite observations increase, and again in 2006, possibly in response to the introduction of data from IASI and GPSRO. Warming by the analysis is evident above 200 hPa and below 700 hPa. In this global view, the mean increments close to the surface exhibit a negative trend with strong warming before the early 1990's turning to slight cooling after 2010, but this is in fact the net effect of distinct regional differences in the increments (not shown). In particular, near-surface warming by the analysis in response to a cold model bias over northern midlatitude land masses is offset by cooling over southern oceans that generally increases with time beginning with the assimilation of data from the first microwave humidity sensors in the late 1980's. These differences also contribute to the large variability of the increments below 700 hPa (Figure 10b). The variability in the mid troposphere is noticeable but small compared with that at low levels, again highlighting the consistency of the cooling by the observations between 250 and 400 hPa.

The increments of specific humidity in the tropics are shown in Figure 11 for levels between the surface and 250 hPa (the values become exceedingly small above this level). The mean increments indicate distinct biases in the middle and lower troposphere, with systematic drying between 600 and 300 hPa, and mostly moistening below 700 hPa. The corrections are generally larger during the second half of the period and especially after the late 1990's as more satellite observations of humidity become available. There is an abrupt increase in the variability of the increments corresponding to the introduction of the first SSM/I instrument in mid 1987, with additional increases corresponding to the use of a second and third SSM/I instrument in late 1990 and mid-1995, respectively. The use of multiple SSM/I instruments from the early 1990's to late 2000's also corresponds to a strong drying and a marked increase in variability at levels very close to the surface. The introduction of AMSU-B data in 1998 corresponds to marked increases in the mean and variability of the increments, the latter being most pronounced in the layer between 800 and 900 hPa. The sensitivity of the precipitation to these observing system changes is discussed in section 5.

4. Aerosol data assimilation

In addition to a standard meteorological analysis, MERRA-2 includes an aerosol analysis as described in Randles et al. (2016, 2017) and Buchard et al. (2017). The multi-decadal coverage and the coupling between aerosols and the circulation is a step forward compared to previous EOS-era reanalyses such as MERRAero, the Navy Aerosol Analysis and Prediction System (NAAPS) reanalysis (Lynch et al. 2016), the Monitoring Atmospheric Composition and Climate (MACC) reanalysis (Inness et al. 2013), and the more recent Copernicus Atmosphere Monitoring Service (CAMS) reanalysis (Flemming et al. 2017). The MERRA-2 system produces 3-hourly analyses and gridded output of both observable

parameters and aerosol diagnostics not easily observed, especially on a global scale, with potential applications ranging from air quality forecasting to studies of aerosol-climate and aerosol-weather interactions (e.g., Bocquet et al. 2015).

An analysis splitting technique (Randles et al. 2017) is used to assimilate aerosol optical depth (AOD) at 550 nm, in which a two-dimensional analysis is performed first using error covariances derived from innovation data and then the horizontal increments are projected vertically and across species using an ensemble method. AOD observations are derived from several sources, including

- Reflectances from AVHRR (1979–2002, ocean-only, Heidinger et al. 2002);
- Reflectances from the Moderate Resolution Imaging Spectroradiometer (MODIS) on Terra (2000-present) and Aqua (2002-present) (Remer et al. 2005; Levy et. al. 2007);
- AOD retrievals from the Multi-angle SpectroRadiometer (MISR) (2000–2014, bright, desert regions only, Kahn et al. 2005);
- Direct AOD measurements from the ground-based Aerosol Robotics Network (AERONE' (1999–2014, Holben et. al. 1998).

MODIS provides the vast majority of AOD observations assimilated in MERRA-2, especially after 2002 when data from both the Terra and Aqua satellites become available. Prior to 2000, only AVHRR reflectances over ocean are used in MERRA-2. AOD for both MODIS and AVHRR are derived from cloud-cleared reflectances using a neural net procedure trained on AERONET measurements (Randles et al. 2017). By construction, these AOD retrievals are unbiased with respect to AERONET observations. AOD from MISR and AERONET observations are used without bias correction. Additional details about the aerosol observing system in MERRA-2 can be found in Randles et al. (2016, 2017).

The Goddard Chemistry, Aerosol, Radiation and Transport model (GOCART; Chin et al. 2002; Colarco et al. 2010) is coupled with the GEOS atmospheric model to simulate the life cycles of five externally-mixed aerosol species, including dust, sea salt, black carbon, organic carbon, and sulfate. The model carries three-dimensional mass mixing ratios of these five aerosol species as prognostic aerosol tracers. The AOD at 550 nm is a column- and species-integrated optical quantity, which is calculated as the summed product of each species mass and its extinction coefficient based on aerosol optical properties derived largely from the Optical Properties of Aerosols and Clouds (OPAC) dataset (see Randles et al. 2017 and references within.) Emissions of both dust and sea salt are wind-driven for each of five size bins, parameterized following Martio-corena and Bergametti (1995) and Gong (2003), respectively. Sulfate and carbonaceous aerosol emissions derive from both natural and anthropogenic sources as described in Randles et al. (2017). In particular, MERRA-2 includes volcanic sources (Diehl et al., 2012) and biomass burning emissions that utilize satellite observations, and are based on the Reanalysis of the Tropospheric chemical composition, version 2 (RETRO-2, Schultz et al. 2008), the Global Fire Emissions Database, version 3.1 (GFED-3.1, van der Werf et al. 2006), and the Quick Fire Emission Dataset, version 2.4r6 (QFED-2.4.r6, Darmenov and da Silva, 2015).

It should be noted that AOD observations can only directly constrain the total, species-integrated and vertically-integrated aerosol extinction — a quantity that can be related to column aerosol mass by assuming a set of optical properties. Non-analyzed aerosol properties such as the vertical distribution, aerosol speciation, and absorption are not fully constrained by the observations and are chiefly determined by the underlying model physics and error covariance assumptions. Despite this fact, Buchard et al. (2017) show that the MERRA-2 aerosol reanalysis has considerable skill in simulating numerous observable aerosol properties. Randles et al. (2017) show that the AOD fields in MERRA-2 generally have both high correlation and low bias relative to independent (non-assimilated) sun-photometer and aircraft observations.

As in the case of the meteorological analysis discussed in section 3, statistics of background and analysis departures provide a basic metric of the quality of the aerosol assimilation. Figure 12 shows probability distribution functions of collocated observation-minus-forecast and observation-minus-analysis departures from MERRA-2 for each sensor in the aerosol observing system. Statistics are shown in terms of the log-transform AOD analysis variable (i.e., ln[AOD + 0.01]) which is approximately normally distributed (Randles et al., 2017). Note that AOD is a dimensionless quantity and log- transformed AOD is typically in the range (−4, 2). As expected, compared to the forecast departures, the analysis departures show reduced bias with respect to the observations. Note also that the innovation variances are much larger over land than ocean, a direct consequence of the signal-to-noise limitation of aerosol retrievals over land.

Regional aspects of the global distribution of aerosols are illustrated in Figure 13, which shows time series of analyzed AOD from MERRA-2 area-averaged over several major aerosol source regions. The contribution of each aerosol species to the total AOD is indicated by the colored shading. The seasonal cycles of dust and biomass burning (carbonaceous) AOD are apparent in all regions. Large increases in sulfate aerosol occur in all regions after the El Chichon (1982) and Pinatubo (1991) volcanic eruptions. Over the Asian region (Figure 13a), the analysis captures high carbonaceous aerosol associated with the 2003 Siberian fires and the increasing trend in AOD between the late 1990s and present (commensurate with increasing anthropogenic aerosol emissions reported by Diehl et al. 2012). The AOD over northern Africa (Figure 13b) is dominated by dust, and major dust transport events such as in 2010 are captured (see Buchard et al. 2017 for details). Carbonaceous aerosol from biomass burning in major source regions such as the Amazon Basin are also well captured (Figure 13c), especially after 2000 when emissions inventories derive from MODIS observations (Darmenov and da Silva, 2015).

Figure 14 compares values of AOD from several recent aerosol reanalyses for the period 2003–2010. Where such information is available, the results are partitioned by species and identified as either fine or coarse mode (see caption for details). Also shown are multi-model average results from Phase I of the Aerosol Comparison (AeroCom) inter-comparison project (Kinne et al. 2006), as well as both model and observational estimates from Yu et al. (2006). The latter study includes an attempt to account for satellite clear-sky biases by combining MODIS and MISR observations with the GOCART model. Compared to MERRAero, for example, MERRA-2 has slightly higher global average AOD due to

increased contributions from dust (related to the assimilation of MISR AOD over bright surfaces) and sea salt (related to changes in model physics). MERRA-2 and NAAPS show similar global average AOD, both for fine and coarse mode aerosol. Models without assimilation (AeroCom and Yu_Model) underestimate global average AOD compared to both observational estimates (Yu_Obs) and the aerosol reanalyses. The MACC aerosol reanalysis has the highest global mean AOD (Bellouin et al. 2013), which is close to the MODIS-only value of 0.188 for the period 2003–2010 (Yu et al. 2006). MACC also has more dust and sea salt aerosol compared to the other reanalyses, particularly over the ocean (not shown).

The direct aerosol impact on the radiative energy balance of Earth is dependent on the vertical distribution of aerosol scattering and absorption, which is not fully constrained by the vertically integrated AOD measurements that MERRA-2 assimilates. An assessment of the aerosol vertical structure and absorption is presented in a companion paper (Buchard et al. 2017). Long-term aerosol reanalyses can potentially reduce uncertainty in how aerosol direct effects have changed over time, particularly once better observational constraints on aerosol absorption become available. The direct radiative effect (DRE) of all aerosols is defined as the flux difference in W m^{-2} between clear- sky and clear clean-sky conditions (no aerosols or clouds). In the absence of clouds, this quantity is less sensitive to the vertical distribution of aerosol absorption, although it remains sensitive to absorbing aerosols over surfaces with high albedo (Chýlek and Coakley, 1974).

Table 4 compares the DRE from MERRA-2, MERRAero, MACC, model inter-comparisons, and the observationally constrained estimate of Yu et al. (2006). Listed are the top-of-the atmosphere (TOA), surface (SFC), and atmospheric (ATM) estimates of DRE for the period 2003–2010, averaged over land and ocean separately. Note that the atmospheric contribution to the DRE is defined as the difference between top-of-the-atmosphere and surface values, ATM = TOA − SFC. Over land, the DRE estimate from MACC best agrees with the observationally-constrained estimate. TOA and SFC forcing in MERRA-2 and MERRAero are lower than in MACC due to their lower AOD, although the atmospheric forcing is similar. Over ocean, the DRE estimates from MERRA-2 and MACC are lower and higher, respectively, than the observational estimate, and both reanalyses have lower estimates of atmospheric absorption. Much of the uncertainty in the DRE reported by the Intergovernmental Panel on Climate Change (IPCC) arises from differences between estimates from global models and satellite-based estimates (Myhre 2009). However, as aerosol reanalyses such as MERRA-2 continue to mature and incorporate additional observations (e.g., from lidars and multi-spectral sensors), we expect a narrowing of the gap between simulated and satellite-based estimates of the DRE.

5. Precipitation

The representation of precipitation in a reanalysis is key to applications in weather and climate as it ties together aspects of both the water and energy cycles. It also presents a significant challenge, however, as estimates of precipitation are only indirectly constrained by observations and are strongly dependent on model physics whose parameterizations have known errors and can be highly sensitive to even small changes in large-scale temperature

and humidity fields. The observations themselves can sometimes introduce additional uncertainty in these estimates as a result of heterogeneous sampling, changes in instrumentation, and time-varying calibration (Bosilovich et al. 2017).

While improved representation of the hydrological cycle was a primary focus of MERRA, the character of its global precipitation in particular was found to be highly sensitive to the assimilated observations and thus to changes in the observing system (e.g., Robertson et al. 2011). Among the development aspects of MERRA-2 intended to address this issue are modifications to GEOS to conserve atmospheric dry mass and ensure that changes in global atmospheric total mass are equivalent to changes in total water (section 2f), exclusion from the analysis of microwave temperature sounding channels with strong surface sensitivity (section 2d) and, less directly, forcing of the land surface by observation-corrected precipitation estimates (section 2g).

a. Global aspects

Bosilovich et al. (2015, 2017) have investigated the global water cycle variability in MERRA-2 using comparisons with observational data sets and other recent reanalyses. Those studies present a broad range of metrics on this topic, a small subset of which are summarized here. Figure 15 shows time series of global mean precipitation for several recent reanalyses and the observation-based estimates from the Global Precipitation Climatology Project (GPCP, Adler et al. 2003). MERRA-2 exhibits larger temporal variability than GPCP but similar temporal variability as other recent reanalyses, and noticeably less spurious temporal variability than MERRA. The largest improvements compared with MERRA in this regard relate to the decreased sensitivity of MERRA-2 to the introduction of AMSU-A radiances on NOAA-15 and −16 in the late 1990s, and to the loss of SSM/I radiances in the late 2000s. There is still an obvious sensitivity in MERRA-2 to the introduction of SSM/I in 1987, but the response to these data is comparable in magnitude to those of the other reanalyses shown. The response in MERRA-2 appears accentuated due to the decrease and subsequent recovery of precipitation through the mid 1980s. This behavior is not reflected in the GPCP time series, but is evident to lesser degrees in CFSR and ERA-Interim, especially after 1983. For MERRA-2 and CFSR, this may be related to the fact that the SST boundary conditions used in these reanalyses reach their global minimum value for the entire reanalysis period after 1985 (Figure 5), but further investigation is required to confirm this. The increasing trend in global precipitation in MERRA-2 from approximately 2.9 mm day^{-1} in 1988 to approximately 3.0 mm day^{-1} in 1998 is likely due to increasing evaporation over oceans driven by the assimilation of additional SSM/I wind speed observations and the tight coupling of evaporation and precipitation in MERRA-2 through the global mass constraint (Bosilovich et al. 2017). Overall, the global mean precipitation values are higher than those of GPCP but well within the envelope of other recent reanalyses.

Spatial comparisons provide additional insight into the strengths and weaknesses of the representation of precipitation globally in MERRA-2. Figure 16 shows maps of time-averaged differences in precipitation during boreal summer for MERRA and MERRA-2 compared with GPCP. MERRA-2 shows general improvement compared to MERRA over

oceanic regions in both the tropics and extratropics, but an increase in positive bias over northern high latitudes. A notable deficiency in MERRA-2 is the excessive precipitation in the vicinity of high topography in the tropics, especially along the Andes and over the maritime continent. This is related to the partitioning between resolved (large scale) and parameterized (convective) precipitation in the MERRA-2 model which, being more heavily skewed toward the former, results in large-scale precipitation over high topography that is difficult to control. In comparing these features with available gauge data, Bosilovich et al. (2015) point out that the maximum precipitation values in MERRA-2 do not always coincide with the maximum terrain height, so that other effects also may play a role locally. Despite this deficiency over tropical land areas, the positive bias over the warm pool present in MERRA is slightly improved in MERRA-2. Additionally, the high precipitation bias over the Central America Sea in MERRA has been reduced significantly in MERRA-2 and precipitation over the Bay of Bengal and Arabian Sea is slightly improved. Results for other seasons (not shown) are qualitatively similar to those in Figure 16.

b. US summertime precipitation variability

Deficiencies in the ability of MERRA to reproduce certain aspects of the summertime seasonal precipitation over the United States (US) have been well documented (Bosilovich 2013). In particular, MERRA was unable to produce seasonal highs and lows in regional precipitation that were similar to observations. For example, droughts and floods were only weakly reproduced.

Figure 17 shows the time series of summertime seasonal precipitation anomalies over the midwestern US as derived from the NOAA Climate Prediction Center (CPC) gauge observations and from MERRA and MERRA-2 model-generated precipitation. (The correlation values between various reanalyses and the gauge data for this and other regions of the US are shown in Figure 18.) The limitations of MERRA are apparent, especially when comparing values for 1988 (regional drought) and 1993 (large-scale flooding) with the observed values. In contrast, MERRA-2 is able to reproduce the 1988 and 1993 anomalies and is generally much better at tracking the overall variability of the observed anomalies. The poor performance of MERRA-2 in 1980 is a notable exception. A significant drought occurred in the southern Great Plains that year, but its location in MERRA-2 extended too far northeastward into the midwestern US.

Figure 18 presents regional summary statistics for US summer seasonal precipitation anomalies for selected reanalyses. The regions are defined as in Bosilovich (2013). For each region, the temporal mean, standard deviation, and anomaly correlation with respect to the CPC data are derived from time series like those shown in Figure 17. In general, precipitation mean values across the US are improved in MERRA-2 compared with MERRA (Figure 18a), and in many regions the values for MERRA-2 improve over those of other reanalyses as well. There is also a marked increase in the standard deviation of the MERRA-2 time series relative to MERRA (Figure 18b). As discussed above, for example, MERRA-2 more realistically reproduces the seasonal extremes in midwestern US precipitation. Note, however, that MERRA-2 overestimates the standard deviation with respect to the CPC estimates in some regions. Ancillary results indicate that this is due to an

excess in the number of days with rain in MERRA-2. Improvements in MERRA-2 are most evident in the anomaly correlation of the seasonal time series (Figure 18c). In this measure, the two most recent reanalyses, JRA-55 and MERRA-2, generally outperform the others. MERRA-2 produces the highest values of the reanalyses shown in most regions, with substantially higher values in a few of these regions.

The detection and analysis of extreme weather, including extreme precipitation events, is a topic of societal interest and another potential application of reanalyses. At least some of this interest is related to assessing changes in the risk of such events in the context of climate change. For example, observation-based studies cite strong evidence of an upward trend in the frequency and intensity of extreme precipitation events averaged over the US during the last 50 years (Kunkel et al. 2013), although the causes of the observed trends are less certain. Figure 19 shows the accumulated precipitation amounts for the largest precipitation events (at the 99th percentile) as derived from gauge observations, MERRA, and MERRA-2. Compared with the observations, MERRA shows very low values, and very little structure across the continental US. MERRA-2, on the other hand, exhibits a spatial pattern more similar to the observations, and the magnitude of the extreme rainfall is also more similar to the observations. MERRA-2 does, however, overestimate the precipitation values over the Midwestern US. While the results in Figure 19 provide an indicator of how the representation of extreme events has improved in MERRA-2 compared with MERRA, the relatively coarse resolution of both reanalyses limits their utility for studying such events in detail. Presumably, the trend toward increasing resolution, among other improvements, will reduce these limitations in future global reanalyses.

6. The stratosphere

In MERRA-2 the stratospheric meteorology and ozone have benefited from improvements to the GEOS atmospheric model and GSI analysis scheme, as well as from the addition of observations that were not incorporated into MERRA. The model changes most relevant to the stratosphere are the use of the cubed sphere grid and the re-tuning of the gravity wave drag (GWD) parameterization. The amplitude of the non-orographic GWD was increased in the tropics, enabling a model-generated Quasi-Biennial Oscillation (QBO) that was not found in the model version used for MERRA (Molod et al. 2015). Having a model-generated QBO, in turn, results in smaller lower-stratospheric analysis wind increments in MERRA-2 than in MERRA (Coy et al. 2016). The strength of the orographic GWD was also increased in the Southern Hemisphere to better model the strong, late-winter westerlies found there (Molod et al. 2015).

The main GSI change relevant to the stratosphere is the use in MERRA-2 of the CRTM for the assimilation of SSU radiances while in MERRA the SSU assimilation was based on GLATOVS (section 2d). These SSU radiance channels are a major source of stratospheric information during the 1980’s and 1990’s, although the SSU instruments during these decades span several satellite platforms, each with different bias characteristics (Kobayashi et al. 2009). The CRTM has been enhanced for SSU data assimilation since MERRA and now accounts for these biasing factors.

The main additional observations relevant to the stratosphere for MERRA-2 are GPSRO bending angle observations from the suite of platforms beginning in July 2004, and temperature and ozone measurements of the middle atmosphere from MLS and OMI on the EOS Aura satellite beginning later the same year (Froidevaux et al. 2006; Schwartz et al. 2008; McPeters et al. 2008). MERRA-2 assimilates GPSRO bending angle observations up to 30 km. Details of the GPSRO platforms assimilated by MERRA-2 can be found in McCarty et al. (2016). The GPSRO observations aid lower stratospheric bias correction by providing a stable source of temperature and moisture measurements. The MLS-retrieved temperature profiles are assimilated in MERRA-2 at altitudes above 5 hPa, providing a strong constraint on the dynamics of the stratopause and lower mesosphere. As shown below in section 6a, this improves the quality of the synoptic meteorological fields at these altitudes but may complicate the study of trends. The MLS and OMI contributions to ozone assimilation are discussed in section 6b.

a. Meteorology

The cubed sphere discretization of the MERRA-2 model eliminates computational instabilities near the poles, a characteristic of latitude-longitude grids. This is especially important for stratospheric analysis where strong cross-polar flow events occur frequently, especially during major sudden warming events, as planetary-scale Rossby waves disturb the polar vortex. Ertel's Potential Vorticity (EPV), a scalar based on the horizontal vorticity, is often used to characterize the stratospheric circulation (Andrews et al. 1987), where stronger EPV gradients imply stronger flow. Figure 20 illustrates a case where the analyzed wind speeds in MERRA-2 reached nearly 170 m s^{-1} close to the polar stratopause on 2 January 1995 at 12 UTC. On a global scale (Figure 20a and b), the MERRA and MERRA-2 EPV fields appear similar, with the polar vortex (indicated by green and orange colors) displaced well off the pole. In both cases, strong winds cross the North Pole as they circle around the region of high EPV. However, a closer look reveals that the EPV in MERRA (Figure 20c) has anomalous radial perturbations near the pole, while the EPV in MERRA-2 (Figure 20d) shows a smooth and strong EPV gradient in this region. Note also that while the largest discontinuities in the MERRA EPV field occur close to the pole itself, their effects can extend well beyond this location.

Figure 21 provides an example of how the assimilation of MLS temperature measurements in MERRA-2 improves the representation of the dynamics near the stratopause. The figure shows the time-height evolution of polar temperatures during the 2005–2006 Northern Hemisphere winter in which a major stratospheric sudden warming occurred. In a comprehensive study of this winter based on MLS observations, Manney et al. (2008) documented the disappearance of the warm polar stratopause during the warming and its later high-altitude reformation and subsequent descent. This breakdown and high-altitude reformation in early February 2006 is now well captured in MERRA-2 (Figure 21b), in contrast to MERRA (Figure 21a).

The characteristics of the assimilation on longer time scales is illustrated in Figure 22, which shows the time-height evolution of global monthly averaged temperature anomalies in MERRA-2. The 35-year mean and annual cycle for the period 1980–2015 have been

subtracted from each pressure level. The global temperatures in the lower stratosphere (100–10 hPa) show no obvious discontinuities as different instruments become available. There is a slight cooling with time over the 35 years, which is generally consistent with recent analyses of the satellite-based stratospheric climate data record (see Seidel et al., 2016 and references therein). There are also episodic temperature increases associated with the two large volcanic eruptions, El Chichon in 1982 and Pinatubo in 1991. In the upper stratosphere, several discontinuities can be seen. There is a marked decrease in temperature near 1 hPa in 1995 when the transition from assimilating NOAA-11 to NOAA-14 SSU channel 3 radiances occurs. The latter are demonstrably cooler (see Figure 16 of McCarty et al. 2016) and are assimilated without bias correction because of the relatively large model errors at this level. There is an overall increase in temperature when AMSU-A data are first assimilated in 1998, which was not as apparent in MERRA (Rienecker et al. 2011) due to the overlapping use of SSU channel 3 and AMSU-A channel 14 radiances in that reanalysis. The overall effect of assimilating the MLS temperature profiles beginning in 2004 is to sharpen the stratopause with warming at approximately 1 hPa and cooling above and below this level.

b. Ozone

The most notable aspects of the MERRA-2 ozone analysis, and those that constitute the main differences with MERRA, are the use of the improved version of SBUV data prior to October 2004 and subsequent assimilation of OMI and MLS observations. The latter provides high vertical resolution (~2.5 km) measurements of stratospheric ozone profiles during both night and day. The specification of background errors for ozone has also been upgraded to account for flow dependent error standard deviations as described in Wargan et al. (2015).

Many ozone data sets exist for various periods between 1980 and present. The decision to use only SBUV, MLS and OMI observations in MERRA-2 was motivated by the desire to avoid introducing multiple discontinuities into the ozone observing system while taking advantage of high-quality data offered by SBUV and EOS Aura retrievals. This approach leads to a relatively homogeneous MERRA-2 ozone record with only one major discontinuity in 2004 when MLS and OMI data replace SBUV observations. The price is a degraded quality of the analyzed ozone during the short periods when the selected data are not available, most notably in the Southern Hemisphere in late 1994, as discussed below.

An initial evaluation of the representation of ozone in MERRA-2 was presented in Bosilovich et al (2015). A more comprehensive validation against independent satellite and ozonesonde data, including evaluation of the vertical structure and variability, is given in Wargan et al. (2017). In particular, it is shown there that the assimilation of MLS observations in MERRA-2 leads to significant improvements in the representation of lower stratospheric ozone when compared with MERRA or compared with the period of SBUV assimilation in MERRA-2. The QBO signal in ozone is discussed in Coy et al. (2016), who demonstrate an improvement in the vertical structure of the ozone QBO signature from 2004 onward, when MLS data are assimilated in MERRA-2. The focus here is on the Antarctic total column ozone in order to illustrate that MERRA-2 has realistic climatic ozone in a

poorly observed region, while also highlighting some of its uncertainties. Two examples are presented: a comparative evaluation of the South Pole ozone in MERRA and MERRA-2 and the representation of Antarctic ozone holes in the present reanalysis. The former follows Wargan et al. (2017).

Figure 23a shows the time series of total ozone derived from ozonesonde measurements at the South Pole, along with MERRA and MERRA-2 output sampled at the ozonesonde times and location between 1986 and 2015. The ozonesonde data, including the integrated column values were obtained from the Earth System Research Laboratory website (http://www.esrl.noaa.gov/gmd/ozwv/ozsondes/spo.html). Note that the vertical range of balloon-borne measurements typically does not extend to pressure levels above 10 hPa and so the upper-stratospheric portion of the column is obtained by extrapolating the mixing ratios from 7 hPa or from the highest observed altitude, whichever is lower. For completeness, Figure 23a also shows the reanalysis data between 1980 and 1985. In the absence of ozonesondes, the reanalyses are sampled four times monthly in one-week intervals for that period. The differences between each reanalysis and the ozonesonde values are plotted in Figure 23b. Overall, both reanalyses capture the annual cycle and much of the interannual variability observed in the ozonesonde data, although there are large discrepancies (greater than 50%) during austral summer months in MERRA-2 prior to 2005 and in MERRA throughout the period of comparison. This is consistent with the fact that the reanalyses are not constrained by SBUV data during polar night. In addition, in late 1994, the SBUV coverage was limited to latitudes north of approximately 30°S owing to an orbital drift of the NOAA-11 satellite, which left the middle and high southern latitudes unobserved in both reanalyses. Nonetheless, these differences are reduced in MERRA-2 compared to MERRA. MERRA-2 performs significantly better than MERRA relative to the South Pole ozonesondes from October 2004 onward, when EOS Aura ozone data are assimilated. In particular, the standard deviation of the differences between MERRA-2 and the ozonesonde values drops from 12.5% between 1991 and 2004 to 5% between 2005 and 2014. At the same time, the correlation between MERRA-2 and the ozonesonde measurements increases from 0.88 to 0.98. The large excursions seen in Figure 23b in MERRA between 2008 and 2012 are due to degraded coverage of the NOAA-17 SBUV instrument. In contrast, the behavior of the MERRA-2 South Pole ozone is remarkably steady relative to the ozonesondes in the period when MLS and OMI data are assimilated. Only small seasonal variations are seen during that period. The MERRA-2 South Pole total ozone exhibits a small negative bias of approximately 6.7 Dobson units (DU), or roughly 2%, throughout the period of comparison. This bias does not vary significantly between the periods when either SBUV or EOS Aura ozone data are assimilated.

As discovered by Molina and Rowland (1974), anthropogenic emissions of chlorofluorocarbons provide the main contribution to the chlorine loading in the stratosphere, leading to destruction of the ozone layer. One prominent feature of the ozone loss in recent decades is the occurrence of springtime ozone holes over Antarctica since the early 1980’s (Farman et al. 1985). Ozone holes are regions of extremely low values of total ozone forming inside the polar vortex due to a series of chlorine-catalyzed reactions (WMO 2014). The climatological importance of this phenomenon warrants its accurate representation in long-term reanalyses. The discussion here focuses on only one simple

diagnostic, the ozone hole area, defined as the region with total ozone values less than 220 DU.

Figure 24 shows the time series of the ozone hole area calculated from the MERRA-2 total ozone averaged between 20 September and 10 October in each year between 1980 and 2015. Also plotted in Figure 24 are the ozone hole area values derived from the Total Ozone Mapping Spectrometer (TOMS) instruments on Nimbus-7 (1980–1992), Meteor-3 (1992–1994) and Earth Probe (1996–2005), and from OMI (2004–2015). Note that OMI data are assimilated in MERRA-2 but TOMS observations are not. With the exception of 1994 there is remarkable agreement between MERRA-2 and these observations. In particular, MERRA-2 realistically captures the ozone hole interannual variability throughout the period of the reanalysis. There is an upward trend between 1980 and the mid-1990s followed by a plateau with the area oscillating around 22×10^6 km^2. This is consistent with the late twentieth century increase of anthropogenic chlorine and bromine loadings and the subsequent slow recovery after the gradual implementation of the Montreal Protocol of 1986 (WMO 2014). The Protocol, which went into effect in the late 1990s, banned the release of the main ozone depleting substances. Because the rate of the springtime polar ozone depletion depends on temperature and the strength of the Antarctic polar vortex in a given year, the size of the ozone hole exhibits a dynamically driven interannual variability superimposed on decadal-scale trends. This dynamical modulation is also evident in Figure 24. The extremely small (less than 3×10^6 km^2) ozone hole in 2002 occurred in conjunction with the only major sudden stratospheric warming in the Southern Hemisphere on record (Newman and Nash 2005).

It should be noted that the southern high-latitude ozone for 1994 in MERRA-2 is not recommended for scientific use. The degraded result for that year is due to limited SBUV data coverage, as explained above, and the decision not to use data sources other than SBUV, OMI and MLS throughout the reanalysis. This particular deficiency is not shared with other major reanalyses (except MERRA), which replaced the missing data with other available observations such as from the short-lived Meteor-3 TOMS instrument (ERA-Interim) or NOAA-9 SBUV (CFSR and JRA-55). The latter were not considered in MERRA-2 because of the poorer quality of its partial columns compared to other SBUV instruments.

Realistic ozone hole interannual variability is also present in MERRA (Sean M. Davis, personal communication 2016) with the exception of 1993, 1994 (as in MERRA-2), and the period between 2010 and 2012 when poor coverage from NOAA-17 SBUV resulted in degraded quality of the Antarctic ozone. The inferior performance of MERRA in 1993 compared to MERRA-2 is a consequence of applying more stringent data quality criteria to the older version of the SBUV data, resulting in limited data coverage near the terminator.

7. Representation of the cryosphere

Reanalyses provide a global context for assessing recent, pronounced high latitude climate variability and provide seamless information on linkages to lower latitudes. As compared to midlatitudes, reanalyses in polar regions are particularly challenged by the paucity of the *in-situ* observational network, by the difficulty of satellite microwave and infrared sensors to

profile the lower atmosphere over snow and ice surfaces, and by an inadequate representation of physical processes in models that are specific to these areas. Of these three challenges, improvement of model representations of physical processes—particularly as they relate to ice and snow surfaces—was seen as the most tractable in the development of MERRA-2.

Several changes in the representation of physical processes between MERRA and MERRA-2 are directly relevant to polar regions. These include the use in MERRA-2 of the cubed-sphere computational grid (e.g., Putman and Lin 2007), which removes the need for gravity wave filtering at high latitudes, as well as daily sea ice concentration and sea surface temperature boundary conditions (Donlon et al. 2012; Reynolds et al. 2007; Taylor et al. 2000), as compared with the weekly fields used in MERRA.

In MERRA, a fixed surface albedo of 0.6 was used with sea-ice cover. This resulted in erroneously warm surface temperatures in the Arctic spring, when the observed albedo is typically much higher (Cullather and Bosilovich 2012). In MERRA-2, Northern Hemisphere sea-ice albedo varies seasonally based on flux tower observations from the Surface Heat Budget of the Arctic Ocean (SHEBA) field experiment (Duynkerke and de Roode 2001). Monthly values are computed and then linearly interpolated in time to produce instantaneous values. Sea-ice albedo in the Southern Hemisphere remains fixed as in MERRA, as there are few reliable albedo observations there. Sea ice in the Southern Hemisphere also does not endure an extended period of surface melting and a resulting decreased albedo as in the Northern Hemisphere. Comparisons with SHEBA observations indicate a substantial reduction in 2-m air temperature biases during boreal spring in MERRA-2.

These comparisons also find a warm bias in winter months over sea ice in MERRA-2 of approximately 1.2°C in comparison to SHEBA. Larger air temperature differences of greater than 3°C are found in comparison to Soviet ice drifting station observations made during the 1980’s (Colony et al. 1992). Simmons et al. (2016) showed that MERRA-2 is an outlier in near-surface temperature trends in polar regions as compared to ERA-Interim, JRA-55, and several conventional data sets. For the period 19802009, annual 2-m air temperatures for the north polar cap bounded by 60°N increased by 0.35 ± 0.08°C per decade in MERRA-2. This is the trend determined from linear regression; the uncertainty denotes the standard error of the trend. By comparison, north polar cap temperatures increased by 0.46 ± 0.09°C per decade in NOAA CFSR, by 0.55 ± 0.10°C per decade in ERA-Interim, and by 0.56 ± 0.09°C per decade in JRA-55. The behavior in MERRA-2 may be attributable to spurious changes in the SST and SIC boundary conditions and the response of the model to changes in surface forcing. Investigation of these issues is ongoing.

A particular focus during the development of MERRA-2 was on the representation of glaciated land surfaces (Cullather et al. 2014). In MERRA, ice sheets had an unrealistic design, with a fixed surface albedo and no representation of surface hydrology. Surface energy fluxes were computed using a fixed sub-surface temperature of 230 K (−43°C). In MERRA-2, energy conduction properties of the upper 15 meters of ice are represented, as well as the energy and hydrologic properties of an overlying, variable snow cover. Snow hydrology follows a modified version of the Stieglitz model that is also used over terrestrial

land surfaces (Lynch-Stieglitz 1994; Stieglitz et al. 2001). This provides an explicit representation of snow densification, meltwater runoff, percolation, refreezing, and a prognostic surface albedo based on Greuell and Konzelmann (1994).

Figure 25 shows the effects of the different surface configurations in MERRA and MERRA-2 on near-surface air temperatures over ice sheets. In MERRA, biases are found when the observed surface temperature differs markedly from the fixed sub-surface temperature of −43°C. This includes South Pole station in winter (Figure 25a), where MERRA values are more than 5 K too warm; over the central Ross Ice Shelf in summer (Figure 25b), where MERRA is 8 K too cold; and over central Greenland in summer (Figure 25c), where MERRA is 4 K too cold. It may be seen from Figure 25 that these seasonal air temperature differences between MERRA and the station values are significant over interannual time periods. In contrast, 2-m air temperatures for these locations in MERRA-2 more closely agree with the observed values.

The surface representation in MERRA-2 also allows for the computation of surface mass balance over ice sheets, which may be defined as the net of precipitation minus evaporation minus runoff. The MERRA system does not provide runoff over land ice and, as seen in Figure 26, lacks ablation areas (in which the annual surface mass balance is negative) along the periphery of the ice sheet. For Greenland these occur mostly as a result of runoff from surface melt. The corresponding fields in MERRA-2, on the other hand, compare well with those from the widely-used Modele Atmospherique Regional regional climate model (MAR; Fettweis 2007), particularly in terms of the accumulation distribution in southeastern and western Greenland and the location of the zero-contour line along the western coast. However, some differences are also evident. For example, the regional climate model indicates average annual mean ablation values of up to 4 m yr^{-1} in southwestern Greenland, as compared with values of approximately 1 m yr^{-1} in MERRA-2. In addition to differing surface representations, differences in grid spacing between MAR (25 km) and MERRA-2 (roughly 50 km) may also play a role. A final point of comparison in Figure 26 is with regard to topography. The MERRA system used a dated topography which contained large errors of up to 600 m over the Greenland Ice Sheet (Box and Rinke 2003). These differences are apparent in the topography contours shown for MERRA and MERRA-2 in Figure 26.

8. MERRA-2 products and access

The complete list of analyzed and diagnosed fields produced by MERRA-2 is given in the product file specification document available at the GMAO's MERRA-2 web site (https://gmao.gsfc.nasa.gov/pubs/docs/Bosilovich785.pdf). The GEOS IAU procedure allows for higher-frequency products than just the 6-hourly ones generated directly from the analysis. There are three time-invariant and 39 time-varying product collections, all produced on a 0.625° × 0.5° horizontal grid. Variables are provided on either the native vertical grid (at 72 model layers or the 73 edges), or interpolated to 42 standard pressure levels. Detailed information and a description of each variable are available in the MERRA-2 file specification document. As in MERRA, MERRA-2 provides closed atmospheric budgets, including the analysis increment terms. The observational forcing from the assimilation

increments during the IAU segment is summed in the output budgets of the model. Bosilovich et al. (2015) show the magnitudes of these terms in water and energy budgets.

The NASA Goddard Earth Sciences Data Information Services Center (GES DISC) provides access to MERRA-2 products through a new unified user interface connected to three different search engines. Many of the tools will be familiar to MERRA users, such as the popular Giovanni visualization and analysis tool, web based FTP servers and OpenDAP web services. The subsetting capability has been updated to include grid transformation options, while retaining the essential functionality of selecting levels, variables, time and domain. Citations for the individual MERRA-2 data collections are included in the GES DISC MERRA-2 data access pages. As noted in section 1, these citations are included in the figure captions of this paper (except where results for MERRA-2 are derived from other sources such as diagnostic output from the data assimilation scheme). Results shown for MERRA are from similarly named data collections, as described by Rienecker et al. (2011).

9. Summary and outlook

The Modern Era Retrospective Analysis for Research Applications Version 2 (MERRA-2) was developed with two primary objectives: to provide an ongoing near-real time climate analysis of the satellite era that addresses known limitations of the now-completed MERRA reanalysis (January 1979-February 2016), and to demonstrate progress toward development of a future integrated Earth system analysis (IESA) capability. MERRA-2 has achieved those objectives in several respects. These include the assimilation of satellite observations not available to MERRA—which assimilated no new satellite observations after NOAA-18 (launched in 2005)—the reduction of certain biases and imbalances in the water cycle, and the reduction of spurious trends and jumps in precipitation related to changes in the observing system. As a step toward a future IESA, MERRA-2 includes aerosol data assimilation and improved representations of aspects of the cryosphere and stratosphere, including ozone, as compared with MERRA.

At the same time, because of the fairly rapid development schedule required to produce a timely replacement for MERRA, other aspects of the MERRA-2 development received less attention. For example, there was little focus on the preparation and improvement of input conventional data types and minimal tuning of the model physics for the current application. Notable shortcomings of MERRA-2 compared with MERRA include an increased warm bias in the upper troposphere—as revealed by the background forecast fit to radiosonde temperature observations and mean analysis increments of temperature—as well as excessive precipitation over high topography in the tropics and, to a lesser extent, over northern high latitudes. Subsequent experimentation indicates that these behaviors are most affected by the model parameterizations of deep convection and gravity wave drag in GEOS, as well as the representation of topography. They are being addressed in more recent model versions.

Ongoing development in other aspects of modeling and data assimilation are likely to provide benefit for reanalyses in the near future. For example, while MERRA-2 assimilates only clear-sky satellite radiances, the use of cloud- and rain-affected radiances—referred to

as all-sky assimilation (Bauer et al. 2010)—has matured or become operational at several centers including GMAO. This should improve the assimilation of moisture- sensitive data types which, as shown here and by Bosilovich et al. (2017), can still induce unexpected changes in global precipitation and moisture fields. Direct assimilation of land surface observations, including remotely sensed soil moisture and snow cover fraction, is another area of improving capability that is likely to provide benefit to reanalysis, especially for capturing extreme events like droughts and heat waves. Implementation of an improved land model that includes dynamic phenology and photosynthesis is a key component of the GMAO's land surface modeling and assimilation efforts (Koster et al. 2014). To improve the specification of ocean surface boundary conditions, many centers are developing some form of coupled ocean-atmosphere analysis system. The GMAO has recently implemented a coupled data assimilation scheme for analyzing ocean skin temperature within the existing atmospheric analysis (Akella et al. 2016). It uses background fields from a near-surface ocean diurnal layer model to assimilate surface-sensitive radiances plus in-situ observations along with all other observations in the atmospheric assimilation system. The scheme may be described as being weakly coupled in the sense that the atmospheric observations do not affect the ocean fields directly, but only through the increment of ocean skin temperature during the next analysis cycle.

Improving the representation of aerosol effects on climate is another important area of development for reanalysis. As the aerosol observing system continues to evolve and provide additional global information on aerosol absorption, size and vertical distribution, the discrepancy among reanalyses and satellite-only estimates of aerosol radiative-climate effects should decrease. For example, the GMAO is working to incorporate aerosol vertical distribution information from space-based lidars, as well as implicit spe- ciation and size information from multi-channel radiometers on low-orbiting and geostationary satellites. Unlike satellite estimates alone, reanalyses like MERRA-2 can provide detailed information on how the anthropogenic component of aerosols, and thus radiative forcing, has changed during the modern satellite era, as well as its interaction with the circulation and the climate at large. This should lead to reduced uncertainty in assessing, for example, the human impact on climate.

More extensive analysis coupling between the atmosphere, ocean, land and chemistry as envisioned for IESA, while progressing, still presents significant challenges (e.g., Brassington et al. 2015). These include model biases that can be exacerbated when coupled, component systems with different physical characteristics and different spatial and temporal scales, and component observations in different media with different spatial and temporal frequencies and different latencies. These challenges may be offset at least partially by the fact that, in practice, where the time scales and observation latencies between components differ greatly—as between the deep ocean and atmosphere for example—a weak coupling approach may suffice. Prospects for success are also bolstered by the fact that the numerical weather prediction community is placing increasing focus on the need to analyze currently uncoupled components of the Earth system in a more consistent manner. The GMAO strategy is to progress incrementally toward an IESA through an evolving combination of coupled systems and offline component reanalyses driven by, for example, MERRA-2 atmospheric forcing.

Quantifying uncertainty in reanalyses remains important for expanding their utility, especially as a potential tool for climate change assessment. Dee et al. (2011) argued that advances in observational bias correction and other aspects of data assimilation have reduced uncertainty in the representation of low-frequency variability to the point where ERA-Interim can be used to estimate certain atmospheric temperature trends. More recently, Simmons et al. (2014) compared multi-annual variability and trends in atmospheric temperature from ERA-Interim, JRA-55 and MERRA and found them to be in generally good agreement in the upper troposphere and lower stratosphere but more uncertain in the middle stratosphere. Nonetheless, for less well constrained quantities such as precipitation and surface fluxes, there still appear to be substantial differences between recent reanalyses. For example, the 12-month running mean values of global precipitation in ERA-Interim, MERRA-2, and JRA-55 can at times differ by almost 20%. Uncertainty in sea surface temperature, as illustrated by the surprising differences between the prescribed values used in different reanalyses (Figure 5) is likely to be a contributing factor. Impacts from observing system changes also appear to play a significant role in explaining these precipitation differences, pointing to the need for new sources of high-quality observations of these or closely related variables not only for assimilation but for improving our understanding and modeling of the underlying physical processes. Ongoing efforts to improve the quality of existing historical data sets are also critical in this regard.

The increasing use of ensemble and hybrid ensemble-variational methods in Earth system data assimilation has the potential to make at least some measures of uncertainty a standard component of reanalysis data sets (e.g., Compo et al. 2011; Poli et al. 2013). The GMAO has recently implemented a hybrid four-dimensional ensemble-variational (4D-ENVAR) assimilation scheme with similar capability. Finally, ECMWF, JMA and GMAO are conducting multi-decadal atmospheric model integrations (without data assimilation) for comparison with reanalyses as a means of assessing internal variability and distinguishing boundary-forced climate signals from those imposed by changes in the observing system. All these efforts will benefit from the continued assessment of existing reanalysis products by the research community, and from the sharing of key data assimilation diagnostic quantities (e.g., background departures, analysis increments, bias estimates) between both reanalysis developers and data providers.

Acknowledgments

Development of the GEOS data assimilation system and the MERRA-2 project were funded by NASA’s Modeling Analysis and Prediction program. Computational resources and support for the execution of MERRA-2 were provided by the NASA High-End Computing Capability Project and NASA Center for Climate Simulation. GEOS and MERRA-2 are the result of years of dedicated research, development and analysis by many individuals at GMAO whose efforts are greatly appreciated. We gratefully acknowledge the GMAO operations group for monitoring the production of MERRA-2 and the GMAO software integration group who helped improve the performance and flexibility of GEOS. We thank Julio Bacmeister for his contribution to the development of the model physics, Qing Liu for processing the precipitation input data, and Allison Collow and Edmond Brent Smith for providing some of the figures for this paper. We also thank the GES DISC for providing on-line access to MERRA-2 products. Finally, we thank the three reviewers, whose comments and suggestions helped improve the paper substantially.

Appendix: Acronyms

3DVAR	Three-dimensional variational data assimilation
4DENVAR	Four-dimensional ensemble-variational data assimilation
AAOD	Aerosol absorption optical depth
ACARS	Aircraft Communications Addressing and Reporting
AeroCom	Aerosol Comparison Project
AERONET	Aerosol Robotics Network
AIREP	Aircraft report
AIRS	Advanced Infrared Sounder
AMDAR	Aircraft Meteorological Data Relay
AMSR-E	Advanced Microwave Scanning Radiometer-EOS
AMSU-A	Advanced Microwave Sounding Unit-A
AMSU-B	Advanced Microwave Sounding Unit-B
AOD	Aerosol optical depth
ASCAT	Advanced Scatterometer
ASDAR	Aircraft to Satellite Data Relay
ATMS	Advanced Technology Microwave Sounder
ATOVS	Advanced TIROS Operational Vertical Sounder
AVHRR	Advanced Very High Resolution Radiometer
CFSR	Climate Forecast System Reanalysis
CAMS	Copernicus Atmosphere Monitoring Service
CMIP	Coupled Model Intercomparison Project
CPC	Climate Prediction Center
CrIS	Cross-track Infrared Sounder
CRTM	Community Radiative Transfer Model
DMSP	Defense Meteorological Satellite Program
DRE	Direct radiative effect
ECMWF	European Centre for Medium-Range Weather Forecasts
EOS	Earth Observing System

ERA-20C	ECMWF Reanalysis from 1900–2010
ERA-Interim	ECMWF Reanalysis from 1979-present
ERS	Environmental Research Satellite
FGAT	First guess at appropriate time
GEOS	Goddard Earth Observing System
GES DISC	Goddard Earth Sciences Data Information Services Center
GLATOVS	Goddard Laboratory for Atmospheres TOVS forward model
GMAO	Global Modeling and Assimilation Office
GMS	Geostationary Meteorological Satellite
GOCART	Goddard Chemistry, Aerosol, Radiation and Transport model
GOES	Geostationary Operational Environmental Satellites
GPCP	Global Precipitation Climatology Project
GPSRO	Global Positioning System radio occultation
GSI	Gridpoint Statistical Interpolation
GWD	Gravity wave drag
HIRS	High-resolution Infrared Radiation Sounder
IASI	Infrared Atmospheric Sounding Interferometer
IAU	Incremental analysis update
IESA	Integrated Earth system analysis
IPCC	Intergovernmental Panel on Climate Change
JMA	Japan Meteorological Agency
JPSS	Joint Polar Satellite System
JRA-55	Japanese 55-year Reanalysis
MACC	Monitoring Atmospheric Composition and Climate project
MAR	Modele Atmospherique Regional regional climate model
MDCRS	Meteorological Data Collection and Reporting System
MERRA	Modern-Era Retrospective Analysis for Research and Applications

MERRA-2	Modern-Era Retrospective Analysis for Research and Applications, Version 2
Metop	Meteorological Operational Satellite
MHS	Microwave Humidity Sounder
MISR	Multi-angle SpectroRadiometer
MLS	Microwave Limb Sounder
MODIS	Moderate Resolution Imaging Spectroradiometer
MSG	Meteosat Second Generation satellite
MSU	Microwave Sounding Unit
MTSAT	Multifunctional Transport Satellite
NAAPS	Navy Aerosol Analysis and Prediction System
NASA	National Aeronautics and Space Administration
NCEP	National Centers for Environmental Prediction
NEXRAD	Next-Generation Radar
NOAA	National Oceanic and Atmospheric Administration
NRL	Naval Research Laboratory
OISST	Optimum Interpolation Sea Surface Temperature
OMI	Ozone Monitoring Instrument
OPAC	Optical Properties of Aerosols and Clouds
OSTIA	Operational Sea Surface Temperature and Sea Ice Analysis
PAOB	Synthetic surface pressure observation
Pibal	Pilot balloon
PIREP	Pilot report
QBO	Quasi-Biennial Oscillation
QFED	Quick Fire Emission Dataset
Raob	Radiosonde observation
RAS	Relaxed Arakawa-Schubert convection scheme
RMS	Root mean square
RSS	Remote Sensing Systems

SBUV	Solar Backscatter Ultraviolet Radiometer
SEVIRI	Spinning Enhanced Visible Infrared Imager
SHEBA	Surface Heat Budget of the Arctic Ocean
SIC	Sea ice concentration
SMAP	Soil Moisture Active Passive satellite
SMOS	Soil Moisture and Ocean Salinity satellite
SNPP	Suomi National Polar-orbiting Partnership
SSM/I	Special Sensor Microwave Imager
SSMIS	Special Sensor Microwave Imager/Sounder
SST	Sea surface temperature
SSU	Stratospheric Sounding Unit
TIROS	Television Infrared Observation Satellite
TLNMC	Tangent linear normal mode constraint
TMI	Tropical Rainfall Measuring Mission Microwave Imager
TOA	Top of the atmosphere
TOMS	Total Ozone Mapping Spectrometer
VAD	Velocity Azimuth Display
WMO	World Meteorological Organization

References

Adler RF, and Coauthors, 2003: The version-2 Global Precipitation Cimatology Project (GPCP) monthly precipitation analysis (1979-present). J. Hydrometeor, 4, 1147–1167.

Akella S, Todling R, M., and Suárez M, 2016: Assimilation for skin SST in the NASA GEOS atmospheric data assimilation system. Quart. J. Roy. Meteor. Soc, doi:10.1002/qj.2988.

Andrews DG, Holton JR, and Leovy CB, 1987: Middle Atmosphere Dynamics. Academic Press, 489 pages.

Bacmeister JT and Stephens G, 2011: Spatial statistics of likely convective clouds in CloudSat data. J. Geophys. Res, 116, D04104, doi:10.1029/2010JD014444.

Ballish BA, and Kumar VK, 2008: Systematic differences in aircraft and radiosonde temperatures. Bull. Amer. Meteor. Soc, 89, 1689–1707.

Bauer P, Geer AJ, Lopez P, and Salmond D, 2010: Direct 4D-Var assimilation of all-sky radiances. Part I: Implementation. Quart. J. Roy. Meteor. Soc, 136, 1868–1885. doi:10.1002/qj.659

Bellouin N, Quaas J, Morcrette J-J and Boucher O, 2013: Estimates of aerosol radiative forcing from the MACC re-analysis. Atmos. Chem. Phys, 13, 2045–2062, doi:10.5194/acp-13-2045-2013.

Berrisford P, Kallberg P, Kobayashi S, Dee D, Uppala S, Simmons AJ, Poli P, and Sato H, 2011: Atmospheric conservation properties in ERA-Interim. Quart. J. Roy. Meteor. Soc, 137, 1381–1399.

Bloom S, Takacs L, DaSilva A, and Ledvina D, 1996: Data assimilation using incremental analysis updates. Mon. Wea. Rev, 124, 1256–1271.

Bocquet M, and Coauthors, 2015:, Data assimilation in atmospheric chemistry models: Current and future prospects for coupled chemistry meteorology models. Atmos. Chem. Phys, 15 (10), 5325–5358, doi:10.5194/acp-15-5325-2015.

Bosilovich MG, 2013: Regional climate and variability in NASA MERRA and recent reanalyses: US summertime precipitation and temperature, J. Appl. Meteor. Climatol, 52, 1939–1951, doi: 10.1175/JAMC-D-12-0291.1.

Bosilovich MG, Robertson FR, and Chen J, 2011: Global energy and water budgets in MERRA. J. Climate, 24, 282–300.

Bosilovich MG, and Coauthors, 2015: MERRA-2: Initial Evaluation of the Climate. NASA/TM2015104606, Vol. 43, 139 pp. https://gmao.gsfc.nasa.gov/pubs/docs/Bosilovich803.pdf.

Bosilovich M, Robertson F, Takacs L, Molod A, and Mocko D, 2017: Atmospheric water balance and variability in the MERRA-2 reanalysis. J. Climate, 30, 1177–1196, doi: 10.1175/JCLI-D-16-0338.1.

Box JE, and Rinke A, 2003: Evaluation of Greenland Ice Sheet surface climate in the HIRHAM regional climate model using automatic weather station data. J. Climate, 16, 1302–1319, doi: 10.1175/1520-0442-16.9.1302.

Brassington GB, Martin MJ, Tolman HL, Akella S, Balmeseda M, Chambers CRS, Cummings JA, Drillet Y, Jansen PAEM, Laloyaux P, Lea D, Mehra A, Mirouze I, Ritchie H, Samson G, Sandery PA, Smith GC, Suárez M, and Todling R, 2015: Progress and challenges in short- to medium-range coupled prediction, J. Op. Oceanogr, 8, 239–258, doi:10.1080/1755876X.2015.1049875.

Buchard V, and Coauthors, 2015: Using the OMI aerosol index and absorption aerosol optical depth to evaluate the NASA MERRA Aerosol Reanalysis. Atmos. Chem. Phys, 15 (10), 5743–5760, 10.5194/acp-15-5743-2015.

Buchard V, Randles CA, da Silva AM, Darmenov A, Colarco PR, Govindaraju R, Ferrare R, Hair J, Beyersdorf AJ, Ziemka LD, and Yu H, 2017: The MERRA-2 Aerosol Reanalysis, 1980-onward, Part 2: Evaluation and case studies. J. Climate, in review.

Cardinali C, Isaksen L, and Anderson E, 2003: Use and impact of automated aircraft data in a global 4DVAR data assimilation system. Mon. Wea. Rev, 131, 1865–1877.

Chen Y, Weng F, Han Y, and Liu Q, 2008: Validation of the community radiative transfer model (CRTM) by using CloudSat Data. J. Geophys. Res, 113 (D8), 2156–2202.

Chin M, Ginoux P, Kinne S, Torres O, Holben BN, Duncan BN, Martin RV, Logan JA, Higurashi A, and Nakajima T, 2002: Tropospheric aerosol optical thickness from the GOCART model and comparisons with satellite and sun photometer measurements. J. Atmos. Sci, 59, 461–483, 10.1175/1520-0469(2002)059<0461:TAOTFT>2.0.CO;2 , 10.1175/1520-0469(2002)059<0461:TAOTFT>2.0.CO;2http://dx.doi.org10.1175/1520-0469(2002)059<0461:TA0TFT>2.0.C0;2, http://dx.doi.org10.1175/1520-0469(2002)059<0461:TA0TFT>2.0.C0;2 .

Chýlek P, and Coakley JA, 1974: Aerosol and climate. Science, 183, 75–77. [PubMed: 17743150]

Colarco P, da Silva A, Chin M, and Diehl T, 2010: Online simulations of global aerosol distributions in the NASA GEOS-4 model and comparisons to satellite and ground-based aerosol optical depth. J. Geophys. Res, 115 (D14207), 10.1029/2009JD012820 , 10.1029/2009JD012820http://dx.doi.org/10.1029/2009JD012820, http://dx.doi.org/10.1029/2009JD012820 .

Collow ABM, Bosilovich MG, and Koster RD, 2016: Large scale influences on summertime extreme precipitation in the northeastern United States. To appear in J. Hydromet, doi: 10.1175/JHM-D-16-0091.1.

Collow ABM, and Miller MA, 2016: The seasonal cycle of the radiation budget and cloud radiative effect in the Amazon rainforest of Brazil. J. Climate, doi: 10.1175/JCLI-D-16-0089.1.

Colony R, Appel I, and Rigor I, 1992: Surface air temperature observations in the Arctic Basin Tech. Memo. TM 1–92, 120 pp. Available from Applied Physics Laboratory, University of Washington, Seattle, WA 98195.

Compo GP, and Coauthors, 2011: The Twentieth Century Reanalysis Project. Quart. J. Roy. Meteor. Soc, 137, 1–28, doi:10.1002/qj.776.

Coy L, Wargan K, Molod AM, McCarty WR, and Pawson S, 2016: Structure and dynamics of the quasi-biennial oscillation in MERRA-2. J. Climate, 29, 5339–5354, doi:10.1175/JCLI-D-15-0809.1.

Cullather RI, and Bosilovich MG, 2012: The energy budget of the polar atmosphere in MERRA. J. Climate, 25, 5–24, doi:10.1175/2011JCLI4138.1.

Cullather RI, Nowicki SMJ, Zhao B, and Suárez MJ, 2014: Evaluation of the surface representation of the Greenland Ice Sheet in a general circulation model. J. Climate, 27, 4835–4856, doi: 10.1175/JCLI-D-13-00635.1.

Darmenov Anton, and da Silva Arlindo, 2015 The Quick Fire Emissions Dataset (QFED): Documentation of versions 2.1, 2.2 and 2.4. NASA/TM2015104606, Vol. 38, 201 pp.

Decker M, Brunke MA, Wang Z, Sakaguchi K, Zeng X, and Bosilovich MG, 2011: Evaluation of the reanalysis products from GSFC, NCEP, and ECMWF using flux tower observations. J. Climate, 24, 221–249, doi:10.1175/JCLI-D-11-00004.1.

Dee DP, and Coauthors, 2011: The ERA-Interim reanalysis: configuration and performance of the data assimilation system. Q. J. R. Meteorol. Soc, 137, 553–597, doi:10.1002/qj.828.

Dee DP, and da Silva AM, 2003: The choice of variable for atmospheric moisture analysis. Mon. Weather Rev, 131 155–171.

Dee D, and Uppala S, 2009: Variational bias correction of satellite radiance data in the ERA-Interim reanalysis. Quart. J. Roy. Meteor. Soc, 135, 1830–1841.

Derber JC, and Wu W-S, 1998: The use of TOVS cloud-cleared radiances in the NCEP SSI analysis system. Mon. Wea. Rev, 126, 2287–2299.

Diehl T, Heil A, Chin M, Pan X, Streets D, Schultz M, and Kinne S, 2012: Anthropogenic, biomass burning, and volcanic emissions of black carbon, organic carbon, and SO2 from 1980 to 2010 for hindcast model experiments. Atmos. Chem. Phys. Discuss, 12 (9), 24 895–24 954, 10.5194/acpd-12-24895-2012 , 10.5194/acpd-12-24895-2012http://www.atmos-chem-phys-discuss.net/12/24895/2012/, http://www.atmos-chem-phys-discuss.net/12/24895/2012/ .

Donlon CJ, Martin M, Stark J, Roberts-Jones J, Fiedler E, and Wimmer W, 2012: The Operational Sea Surface Temperature and Sea Ice Analysis (OSTIA) system. Remote Sens. Environ, 116, 140–158, doi:10.1016/j.rse.2010.10.017.

Draper C, Reichle R, and Koster R, 2017: Assessment of the MERRA-2 land surface energy flux estimates. J. Climate, in review.

Duynkerke P, and de Roode S, 2001: Surface energy balance and turbulence characteristics observed at the SHEBA Ice Camp during FIRE III. J. Geophys. Res, 106, 15313–15322, doi: 10.1029/2000JD900537.

Farman J, Gardiner B, B., and Shanklin J, 1985: Large losses of total ozone in Antarctica reveal seasonal ClOx/NOx interaction Nature, 315 (6016), 207–210, doi: 10.1038/315207a0.

Fettweis X, 2007: Reconstruction of the 1979–2006 Greenland ice sheet surface mass balance using the regional climate model MAR. The Cryosphere, 1, 21–40, doi:10.5194/tc-1-21-2007.

Flemming J, Benedetti A, Inness A, Engelen R, Jones L, Huijnen V, Remy S, Parrington M, Suttie M, Bozzo A, Peuch V-H, Akritidis D, and Katragkou E, 2017: The CAMS interim Reanalysis of Carbon Monoxide, Ozone and Aerosol for 2003–2015, Atmos. Chem. Phys, 17, 1945–1983, doi: 10.5194/acp-17-1945-2017.

Froidevaux L, and Coauthors, 2006: Early validation analyses of atmospheric profiles from EOS MLS on the Aura satellite. IEEE Transactions on Geoscience and Remote Sensing 44, no. 5, doi: 10.1109/TGRS.2006.864366.

Global Modeling and Assimilation Office (GMAO), 2015a: MERRA-2 instl_2d_asm_Nx: 2d, 3-Hourly, Instantaneous, Single-Level, Assimilation, Single-Level Diagnostics V5.12.4, Greenbelt, MD, USA, Goddard Earth Sciences Data and Information Services Center (GES DISC), accessed June 2016, doi:10.5067/3Z173KIE2TPD.

Global Modeling and Assimilation Office (GMAO), 2015b: MERRA-2 instl_2dJnt_Nx: 2d,1-Hourly, Instantaneous, Single-Level, Assimilation, Vertically Integrated Diagnostics V5.12.4, Greenbelt, MD, USA, Goddard Earth Sciences Data and Information Services Center (GES DISC), accessed June 2016, doi:10.5067/G0U6NGQ3BLE0.

Global Modeling and Assimilation Office (GMAO), 2015c: MERRA-2 inst3_3d_asm_Np: 3d, 3-Hourly, Instantaneous, Pressure-Level, Assimilation, Assimilated Meteorological Fields, V5.12.4, Greenbelt, MD, USA: Goddard Space Flight Center Distributed Active Archive Center (GSFC DAAC), accessed June 2016, doi:10.5067/QBZ6MG944HW0.

Global Modeling and Assimilation Office (GMAO), 2015d: MERRA-2 tavgl_2d_flx_Nx: 2d, 1-Hourly, Time-Averaged, Single-Level, Assimilation, Surface Flux Diagnostics V5.12.4, Greenbelt, MD, USA, Goddard Earth Sciences Data and Information Services Center (GES DISC), accessed June 2016, doi:10.5067/7MCPBJ41Y0K6.

Global Modeling and Assimilation Office (GMAO), 2015e: MERRA-2 tavgl_2dJnt_Nx: 2d, 1-Hourly, Time-Averaged, Single-Level, Assimilation, Vertically Integrated Diagnostics V5.12.4, Greenbelt, MD, USA, Goddard Earth Sciences Data and Information Services Center (GES DISC), accessed June 2016, doi:10.5067/Q5GVUVUIVGO7.

Global Modeling and Assimilation Office (GMAO), 2015f: MERRA-2 tavgl_2d_slv_Nx: 2d, 1-Hourly, Time-Averaged, Single-Level, Assimilation, Single-Level Diagnostics V5.12.4, Greenbelt, MD, USA, Goddard Earth Sciences Data and Information Services Center (GES DISC), accessed June 2016, doi:10.5067/VJAFPLI1CSIV.

Global Modeling and Assimilation Office (GMAO), 2015g: MERRA-2 tavgM_2d_aer_Nx: 2d, Monthly mean, Time-averaged, Single-Level, Assimilation, Aerosol Diagnostics V5.12.4, Greenbelt, MD, USA: Goddard Space Flight Center Distributed Active Archive Center (GSFC DAAC), accessed June 2016, doi:10.5067/FH9A0MLJPC7N.

Global Modeling and Assimilation Office (GMAO), 2015h: MERRA-2 tavgM_2d_flx_Nx: 2d, Monthly mean, Time-Averaged, Single-Level, Assimilation, Surface Flux Diagnostics V5.12.4, Greenbelt, MD, USA, Goddard Earth Sciences Data and Information Services Center (GES DISC), accessed June 2016, doi:10.5067/0JRLVL8YV2Y4.

Global Modeling and Assimilation Office (GMAO), 2015i: MERRA-2 tavgM_2d_glc_Nx: 2d, Monthly mean, Land Ice Surface Diagnostics, V5.12.4, Greenbelt, MD, USA: Goddard Space Flight Center Distributed Active Archive Center (GSFC DAAC), accessed June 2015, doi: 10.5067/5W8Q3I9WUFGX.

Global Modeling and Assimilation Office (GMAO), 2015j: MERRA-2 tavgM_2ddnd_Nx: 2d, Monthly mean, Land Surface Diagnostics, V5.12.4, Greenbelt, MD, USA: Goddard Space Flight Center Distributed Active Archive Center (GSFC DAAC), accessed June 2015, doi: 10.5067/8S35XF81C28F.

Global Modeling and Assimilation Office (GMAO), 2015k: MERRA-2 tavgM_2d_int_Nx: 2d, Monthly mean, Time-Averaged, Single-Level, Assimilation, Vertically Integrated Diagnostics V5.12.4, Greenbelt, MD, USA, Goddard Earth Sciences Data and Information Services Center (GES DISC), accessed June 2015, doi:10.5067/FQPTQ4OJ22TL.

Global Modeling and Assimilation Office (GMAO), 2015l: MERRA-2 tavgM_3d_qdt_Np: 3d, Monthly mean, Time-Averaged, Pressure-Level, Assimilation, Moist Tendencies V5.12.4, Greenbelt, MD, USA, Goddard Earth Sciences Data and Information Services Center (GES DISC), accessed June 2016, doi:10.5067/2ZTU87V69ATP.

Global Modeling and Assimilation Office (GMAO), 2015m: MERRA-2 tavgM_2d_slv_Nx: 2d, Monthly mean, Single-Level Diagnostics, V5.12.4, Greenbelt, MD, USA: Goddard Space Flight Center Distributed Active Archive Center (GSFC DAAC), accessed April 2015, doi:10.5067/AP1B0BA5PD2K.

Global Modeling and Assimilation Office (GMAO), 2015n: MERRA-2 tavgM_3d_tdt_Np: 3d, Monthly mean, Time-Averaged, Pressure-Level, Assimilation, Temperature Tendencies V5.12.4, Greenbelt, MD, USA, Goddard Earth Sciences Data and Information Services Center (GES DISC), accessed June 2016, doi:10.5067/VILT59HI2MOY.

Gong SL, 2003: A parameterization of sea-salt aerosol source function for sub- and super-micron particles. Global Biogeochemical Cycles, 17 (4), doi:10.1029/2003GB002079.

Greuell W, and Konzelmann T, 1994: Numerical modelling of the energy balance and englacial temperature of the Greenland Ice Sheet. Calculations for the ETH-Camp location (West Greenland, 1155m a.s.l.). Global Planet. Change, 9, 91–114, doi:10.1016/0921-8181(94)90010-8.

Ham Y-G, Schubert S, Vikhliaev Y, and Suárez MJ, 2014: An assessment of the ENSO forecast skill of GEOS-5 system. Clim. Dynam, doi:10.1007/s00382-014-2063-2.

Han Y, van Delst P, Liu Q, Weng F, Yan B, Treadon R, and Derber J, 2006: JCSDA Community Radiative TransferModel (CRTM)-Version 1. NOAA Tech. Rep. 122, 33 pp.

Heidinger AK, Cao C, and Sullivan JT, 2002: Using Moderate Resolution Imaging Spectrometer (MODIS) to calibrate Advanced Very High Resolution Radiometer reflectance channels. J. Geophys. Res. Atmos, 107 (D23), 10.1029/2001JD002035 , 10.1029/2001JD002035http://dx.doi.org/10.1029/2001JD002035, http://dx.doi.org/10.1029/2001JD002035 .

Hoch SW, 2005: Radiative flux divergence in the surface boundary layer. A study based on observations at Summit, Greenland Ph.D. dissertation, Swiss Federal Institute of Technology (ETH), Zurich, 164 pp.

Holben B, and Coauthors, 1998: AERONET - A federated instrument network and data archive for aerosol characterization. Remote Sens. Environ, 66 (1), 1–16, http://dx.doi.org/10.1016/S0034-4257(98)00031-5 , http://dx.doi.org/10.1016/S0034-4257(98)00031-5http://www.sciencedirect.com/science/article/pii/S0034425798000315, http://www.sciencedirect.com/science/article/pii/S0034425798000315 .

Holm EV, 2003: Revision of the ECMWF humidity analysis: Construction of a Gaussian control variable. In Proceedings of Workshop on Humidity Analysis, 1–3. ECMWF/GEWEX: Reading, UK.

Inness A, Baier F, Benedetti A, Bouarar I, Chabrillat S, Clark H, H., and Coauthors, 2013: The MACC reanalysis: An 8 yr data set of atmospheric composition. Atmos. Chem. Phys, 13, 4073–4109, doi:10.5194/acp-13-4073-2013.

Kahn RA, Gaitley BJ, Martonchik JV, Diner DJ, Crean KA, and Holben B, 2005: Multiangle Imaging Spectroradiometer (MISR) global aerosol optical depth validation based on 2 years of coincident Aerosol Robotic Network (AERONET) observations. J. Geophys. Res. Atmos, 110 (D10), 10.1029/2004JD004706, URL 10.1029/2004JD004706.

Kleist DT, Parrish DF, Derber JC, Treadon R, Errico RM, and Yang R, 2009a: Improving incremental balance in the GSI 3DVAR analysis system. Mon. Wea. Rev, 137, 1046–1060.

Kleist DT, Parrish DF, Derber JC, Treadon R, Wu W-S, and Lord S, 2009b: Introduction of the GSI into the NCEPs Global Data Assimilation System. Wea. Forecasting, 24, 1691–1705.

Kinne S, and Coauthors, 2006:, An AeroCom initial assessment - optical properties in aerosol component modules of global models. Atmos. Chem. Phys, 6, 1815–1834, doi:10.5194/acp-6-1815-2006.

Kobayashi S, Matricardi M, Dee D, and Uppala S, 2009: Toward a consistent reanalysis of the upper stratosphere based on radiance measurements from SSU and AMSU-A. Quart. J. Roy. Meteor. Soc, 135, 2086–2099, doi:10.1002/qj.514.

Kobayashi S, Ota Y, Harada Y, Ebita A, Moriya M, Onoda H, Onogi K, Kamahori H, Kobayashi C, Endo H, Miyaoka K, and Takahashi K, 2015: The JRA-55 reanalysis: General specifications and basic characteristics. J. Meteorol. Soc. Japan, 93 (1), 5–48. doi:10.2151/jmsj.2015-001.

Koster RD, Walker G, Collatz GJ, and Thornton PE, 2014: Hydroclimatic controls on the means and variability of vegetation phenology and carbon uptake. J. Climate, 27, 5632–5652. doi: 10.1175/JCLI-D-13-00477.

Kunkel KE, and Coauthors, 2013: Monitoring and understanding trends in extreme storms: State of knowledge. Bull. Amer. Meteor. Soc, 94, 499–514, doi:10.1175/BAMS-D-11-00262.1.

Levy RC, Remer LA, Mattoo S, Vermote EF, and Kaufman YJ, 2007: Second-generation operational algorithm: Retrieval of aerosol properties over land from inversion of Moderate Res- olution Imaging Spectroradiometer spectral reflectance. J. Geophys. Res. Atmos, 112 (D13), 10.1029/2006JD007811, URL 10.1029/2006JD007811.

Lim Y-K, Kovach R, Pawson S, and Vernieres G, 2017: The 2015/2016 El Nino event in context of the MERRA-2 reanalysis: A comparison of the tropical Pacific with 1982/1983 and 1997/1998. J. Climate, doi:10.1175/JCLI-D-16-0800.1, in press.

Liu Q and Boukabara S, 2014: Community Radiative Transfer Model (CRTM) applications in supporting the Suomi National Polar-orbiting Partnership (SNPP) mission validation and verification. Remote Sens. Environ, 140, 744–754.

Lynch P, and Coauthors, 2016:, An 11-year global gridded aerosol optical thickness reanalysis (v1.0) for atmospheric and climate sciences. Geosci. Model Dev, 9, 1489–1522, doi:10.5194/gmd-9-1489-2016.

Lynch-Stieglitz M, 1994: The development and validation of a simple snow model for the GISS GCM. J. Climate, 7, 1842–1855, doi:10.1175/1520-0442(1994)007,1842:TDAVOA.2.0.CO;2.

Manney GL, Kruger K, Pawson S, Minschwaner K, Schwartz MJ, Daffer WH, Livesey NJ, Mlynczak MG, Remsberg EE, Russell JM, Waters JW, 2008: The evolution of the stratopause during the 2006 major warming: Satellite data and assimilated meteorological analyses. J. Geophys. Res, 113, D11115, doi:10.1029/2007JD00909.

Marticorena B, and Bergametti G, 1995: Modeling the atmospheric dust cycle: 1. Design of a soil-derived dust emission scheme. J. Geophys. Res. Atmos, 100 (D8), 16415–16430, doi: 10.1029/95JD00690.

McCarty W, Coy L, Gelaro R, Huang A, Merkova D, Smith EB, Sienkiewicz M, and Wargan K, 2016: MERRA-2 input observations: Summary and initial assessment. NASA Technical Report Series on Global Modeling and Data Assimilation, NASA/TM-2016–104606, Vol. 46, 61 pp.

McPeters R, Kroon M, Labow G, Brinksma E, Balis D, Petropavlovskikh I, Veefkind JP, Bhartia PK, and Levelt PF, 2008: Validation of the Aura Ozone Monitoring Instrument total column ozone product. J. Geophys. Res, 113, D15S14, doi:10.1029/2007JD008802.

Meng J, Yang R, Wei H, Ek M, Gayno G, Xie P, and Mitchell K, 2012: The Land Surface Analysis in the NCEP Climate Forecast System Reanalysis. J. Hydrometeor, 13, 1621–1630, doi: 10.1175/JHM-D-11-090.1.

Mesinger F, and Coauthors, 2006: North American Regional Reanalysis. Bull. Amer. Meteor. Soc, 87, 343–360, doi:10.1175/BAMS-87-3-343.

Molina MJ, and Rowland FS, 1974: Stratospheric sink for chlorouoromethanes: Chlorine atom-catalysed destruction of ozone. Nature, 249 (28), 810–812.

Molod A, Takacs L, Suárez M, and Bacmeister J, 2015: Development of the GEOS-5 atmospheric general circulation model: evolution from MERRA to MERRA2, Geosci. Model Dev., 8, 1339–1356, doi:10.5194/gmd-8-1339-2015.

Moorthi S, and Suárez MJ, 1992: Relaxed Arakawa-Schubert: A parameterization of moist convection for general circulation models. Mon. Wea. Rev, 120, 978–1002.

Newman PA, and Nash ER, 2005: The unusual southern hemisphere stratosphere winter of 2002. J. Atmos. Sci, 62, 614–628, doi: 10.1175/JAS-3323.1.

Myhre G, 2009:, Consistency between satellite-derived and modeled estimates of the Direct Aerosol Effect. Science, 325, 187–190. [PubMed: 19541952]

Parrish DF, and Derber JC, 1992: The National Meteorological Center's spectral statistical-interpolation analysis system. Mon. Wea. Rev, 120, 1747–1763. 10.1175/1520-0493(1992)120¡1747:TNMCSS¿2.0.CO;2

Poli P, and Coauthors, 2013: The data assimilation system and initial performance evaluation of the ECMWF pilot reanalysis of the 20th-century assimilating surface observations only (ERA-20C). ERA Report Series 14

Putman W and Lin S-J, 2007: Finite Volume Transport on Various Cubed Sphere Grids. J. Comput. Phys, 227, 55–78. doi:10.1016/j.jcp.2007.07.022.

Randles CA, da Silva AM, Buchard V, Darmenov A, Colarco PR, Aquila V, Bian H, Nowottnick EP, Pan X, Smirnov A, Yu H, and Govindaraju R, 2016: The MERRA-2 aerosol assimilation. NASA Technical Report Series on Global Modeling and Data Assimilation, NASA/TM-2016–104606, Vol. 45, 143 pp.

Randles CA, da Silva A, Buchard V, Colarco PR, Darmenov A, Govindaraju R, Smirnov A, Holben B, Ferrare R, Hair J, Shinozuka Y, and Flynn CJ, 2017: The MERRA-2 Aerosol Reanalysis, 1980-onward, Part 1: System description and data assimilation evaluation. J. Climate, in review.

Reichle RH, Koster RD, De Lannoy GJM, Forman BA, Liu Q, Mahanama S, and Toure A, 2011: Assessment and enhancement of MERRA land surface hydrology estimates. J. Climate, 24, 6322–6338. doi:10.1175/JCLI-D-10-05033.1.

Reichle RH, and Liu Q, 2014: Observation-Corrected Precipitation Estimates in GEOS-5. NASA/TM2014–104606, Vol. 35.

Reichle RH, Draper CS, Liu Q, Girotto M, Mahanama SPP, Koster RD, and De Lannoy GJM, 2017b: Assessment of MERRA-2 land surface hydrology estimates, J. Climate, doi:10.1175/JCLI-D-16-0720.1.

Reichle RH, Liu Q, Koster RD, Draper CS, Mahanama SPP, and Partyka GS, 2017a: Land surface precipitation in MERRA-2, J. Climate, 30, 16431664, doi:10.1175/JCLI-D-16-0570.1.

Remer LA, and Coauthors, 2005: The MODIS aerosol algorithm, products, and validation. J. Atmos. Sci, 62, 947–973, 10.1175/JAS3385.1 , 10.1175/JAS3385.1http://dx.doi.org/10.1175/JAS3385.1, http://dx.doi.org/10.1175/JAS3385.1 .

Reynolds RW, Rayner NA, Smith TM, Stokes DC, and Wang W, 2002: An improved in situ and satellite SST analysis for climate. J. Climate, 15, 1609–1625.

Reynolds RW, Smith TM, Liu C, Chelton DB, Casey KS, and Schlax MG, 2007: Daily high-resolution-blended analyses for sea surface temperature. J. Climate, 20, 5473–5496, doi: 10.1175/2007JCLI1824.1.

Rienecker MM, and Coauthors, 2008: The GEOS-5 Data Assimilation System- Documentation of versions 5.0.1 and 5.1.0, and 5.2.0. NASA Technical Report Series on Global Modeling and Data Assimilation, NASA/TM-2008–104606, Vol. 27, 118 pp. https://gmao.gsfc.nasa.gov/pubs/docs/Rienecker369.pdf.

Rienecker and Coauthors, 2011: MERRA - NASA's Modern-Era Retrospective Analysis for Research and Applications. J. Climate, 24, 3624–3648, doi:10.1175/JCLI-D-11-00015.1.

Robertson FR, Bosilovich MG, Chen J, and Miller TL, 2011: The effect of satellite observing system changes on MERRA water and energy fluxes. J. Climate, 24, 5197–5217. doi: 10.1175/2011JCLI4227.1.

Saha S, and Coauthors, 2010: The NCEP Climate Forecast System Reanalysis. Bull. Amer. Meteor. Soc, 91, 1010–1057, doi:10.1175/2010BAMS3001.1.

Schubert SD, Rood R, and Pfaendtner J, 1993: An assimilated dataset for earth science applications. Bull. Amer. Meteor. Soc, 74, 2331–2342, doi:10.1175/1520-0477(1993)0742.0.CO;2.

Schultz MG, Heil A, Hoelzemann JJ, Spessa A, Thonicke K, Goldammer J, Held AC, Pereira JM, and van het Bolscher M, 2008: Global Wildland Fire Emissions from 1960 to 2000. Global Biogeochem. Cyc, 22, GB2002, doi:10.1029/2007GB003031.

Schwartz MJ, and Coauthors, 2008: Validation of the Aura Microwave Limb Sounder temperature and geopotential height measurements. J. Geophys. Res 113, D15S11, doi:10.1029/2007JD008783.

Segal-Rosenhemier M, Barton N, Redmann J, Schmidt S, LeBlanc S, Anderson B, Winstead E, Corr C, Moore R, Thornhill LK, and Cullather RI., 2017: Improving our understanding of surface radiative flux bias in Arctic reanalysis over the marginal ice zone: Observational based sensitivity analysis during ARISE. J. Clim, in review.

Seidel DJ, Li J, Mears C, Moradi I, Nash J, Randel WJ, Saunders R, Thompson DWJ, and Zou C-Z, 2016: Stratospheric temperature changes during the satellite era. J. Geophys. Res. Atmos, 121, doi:10.1002/2015JD024039.

Simmons AJ, Berrisford P, Dee DP, Hersbach H, Hirahara S, and Thpaut J-N, 2016: A reassessment of temperature variations and trends from global reanalyses and monthly surface climatological datasets. Quart. J. Roy. Meteor. Soc, doi10.1002/qj.2949.

Simmons AJ, Poli P, Dee DP, Berrisford P, Hersbach H, Kobayashi S, and Peubey C, 2014: Estimating low-frequency variability and trends in atmospheric temperature using ERA-Interim. Q. J. R. Meteorol. Soc, 140, 329–353, doi:10.1002/qj.2317.

Stieglitz M, Ducharne A, Koster RD, and Suárez MJ, 2001: The impact of detailed snow physics on the simulation of snow cover and subsurface thermodynamics at continental scales. J. Hydrometeor, 2, 228–242, doi:10.1175/1525-7541(2001)002,0228:TI0DSP.2.0.C0;2.

Susskind J, Rosenfield J, and Reuter D, 1983: An accurate radiative transfer model for use in the direct physical inversion of HIRS and MSU temperature sounding data. J. Geophys. Res, 88, 8550–8568.

Takacs LL, Suárez MJ, and Todling R, 2016: Maintaining atmospheric mass and water balance in reanalyses. Quart. J. Roy. Meteor. Soc, 142 1565–1573. doi: 10.1002/qj.2763.

Taylor KE, Williamson D, and Zwiers F, 2000: The sea surface temperature and sea ice concentration boundary conditions for AMIP II simulations Program for Climate Model Diagnosis and Intercomparison (PCMDI). Report 60, Lawrence Livermore National Laboratory.

Trenberth KE, and Smith L, 2005: The mass of the atmosphere: A constraint on global analysis. J. Climate, 18, 864–875.

Turner J, Colwell S, Marshall G, Lachlan-Cope T, Carleton A, Jones P, Lagun V, Reid P, and Iagovkina S, 2004: The SCAR READER Project: Toward a High- Quality Database of Mean Antarctic Meteorological Observations. J. Climate, 17, 2890–2898, doi: 10.1175/1520-0442(2004)017<2890:TSRPTA>2.0.C0;2.

van der Werf GR, Randerson JY, Giglio L, Collatz GJ, Kasibhatla PS, and Arellano AF Jr., 2006: Interannual variability in global biomass burning emissions from 1997 to 2004. Atmos. Chem. Phys, 6, 3423–3441, doi:10.5194/acp-6-3423-2006.

Wargan K, and Coy L, 2016: Strengthening of the Tropopause Inversion Layer during the 2009 Sudden Stratospheric Warming: A MERRA-2 Study. J. Atmos. Sci, 73, 1871–1887, doi: 10.1175/JAS-D-15-0333.1

Wargan K, Labow G, Frith S, Pawson S, and Partyka G, 2017: Evaluation of the ozone fields in NASAs MERRA-2 reanalysis. J. Climate, doi: 10.1175/JCLI-D-16-0699.1.

Wargan K, Pawson S, Olsen MA, Witte JC, Douglass AR, Ziemke JR, Strahan SE, and Nielsen JE, 2015: The global structure of upper troposphere-lower stratosphere ozone in GEOS-5: A multiyear assimilation of EOS Aura data, J. Geophys. Res. Atmos, 120, 2013–2036, doi: 10.1002/2014JD022493.

World Meteorological Organization (WMO 2014): Scientific Assessment of Ozone Depletion: 2014. Global Ozone Research and Monitoring Project - Report no. 55.

Wu W-S, Purser RJ, and Parrish DF, 2002: Three-dimensional variational analysis with spatially inhomogeneous covariances. Mon. Wea. Rev, 130, 2905–2916.

Xie P, Yatagai A, Chen M, Hayasaka T, Fukushima Y, Liu C, and Yang S, 2007: A gauge-based analysis of daily precipitation over East Asia. J. Hydrometeorol, 8, 607–626.

Yu H, and Coauthors, 2006: A review of measurement-based assessments of the aerosol direct radiative effect and forcing. Atmos. Chem. Phys, 6, 613–666, doi:10.5194/acp-6-613-2006.

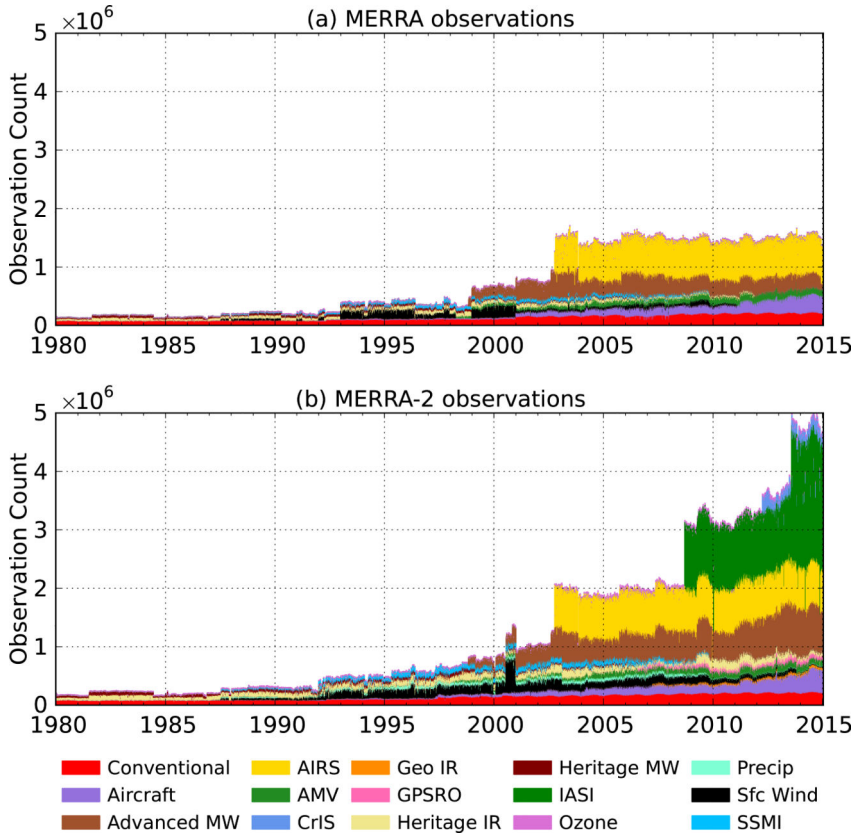

Figure 1:

Observations assimilated per 6-hr cycle in (a) MERRA and (b) MERRA-2. The temporary spike in the number of surface wind observations assimilated in MERRA-2 in late 2000 is due to an error in the pre-processing of QuikSCAT data.

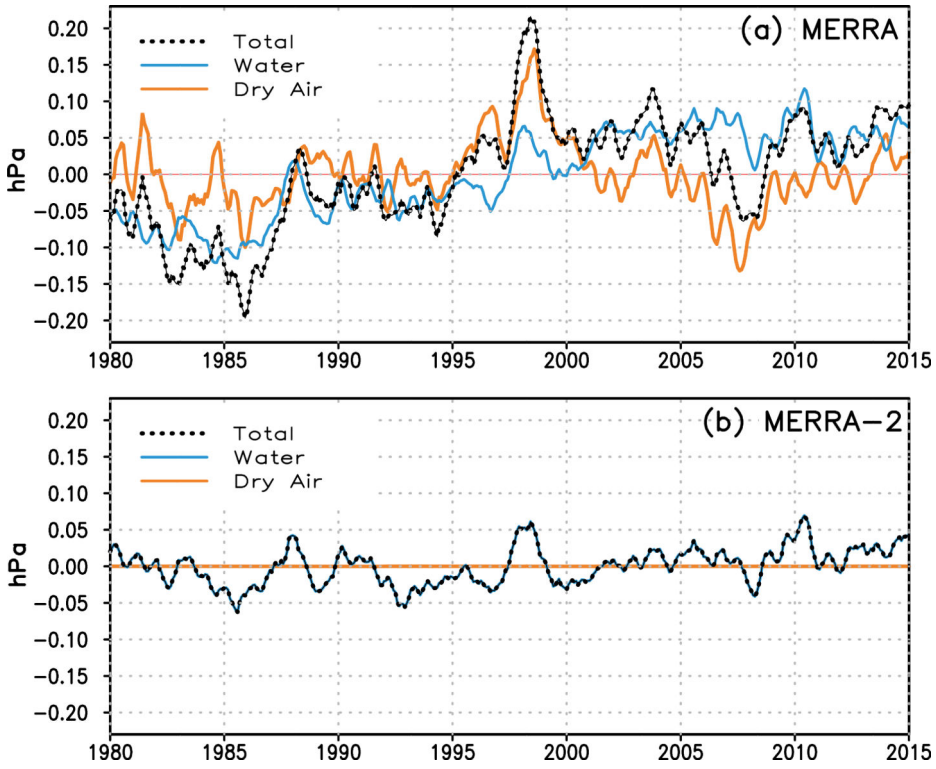

Figure 2:

Globally integrated monthly-mean mass anomalies from the mean seasonal cycle for (a) MERRA and (b) MERRA-2. Shown are the anomalies of total mass (black dotted), and their decomposition into atmospheric water (blue) and dry air (orange). The units are hPa. Results for MERRA-2 are derived from the data collection described in GMAO (2015b).

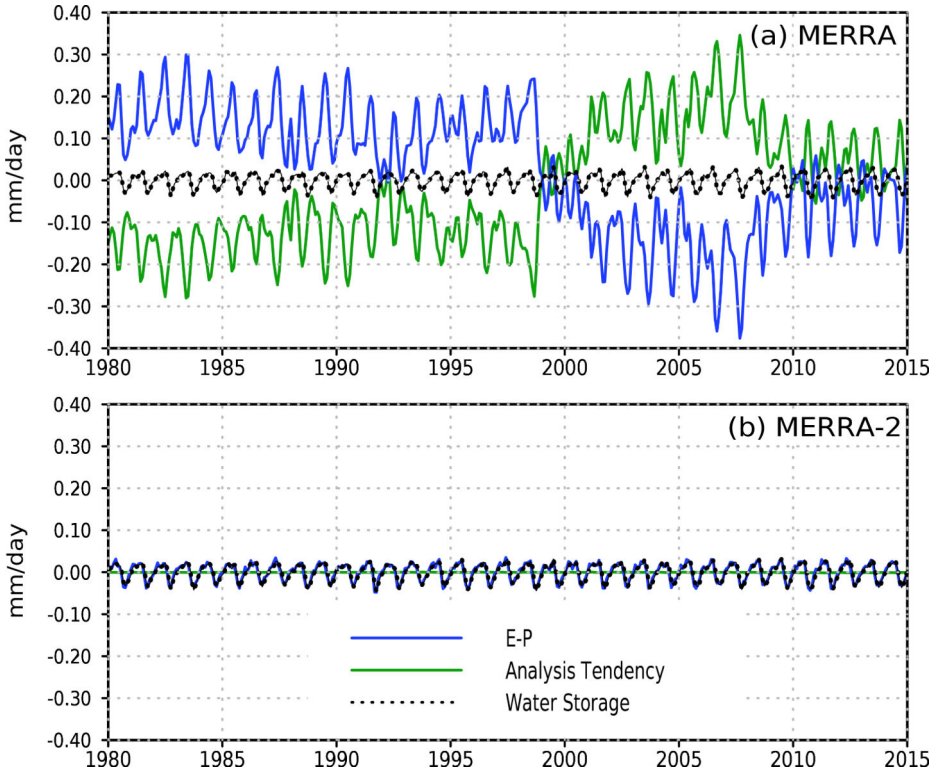

Figure 3:

Globally integrated monthly-mean total water budget terms for (a) MERRA and (b) MERRA-2. Shown are the water source term ($E - P$, blue), vertically integrated analysis increment of water (green), and atmospheric water storage (black dotted). The units are mm day^{-1}. Results for MERRA-2 are derived from the data collections described in GMAO (2015b, d, e).

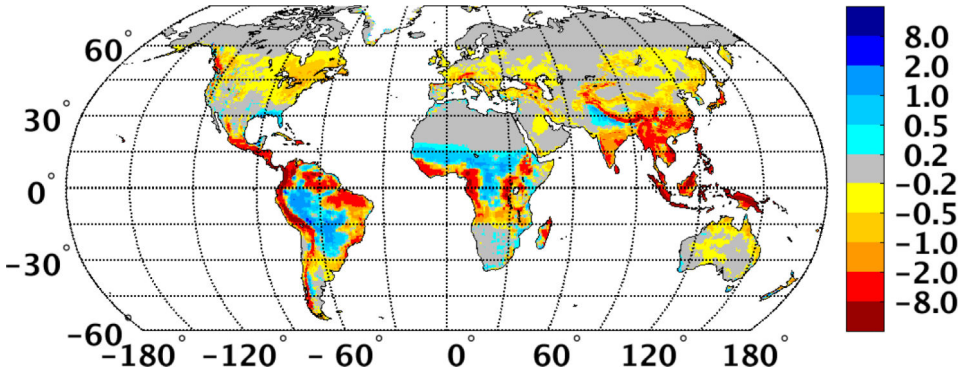

Figure 4:

Mean difference (1980–2015) between the (corrected) MERRA-2 precipitation seen by the land surface and the model-generated precipitation within the MERRA-2 system. The units are mm d^{-1}. Results are derived from the data collections described in GMAO (2015h, j).

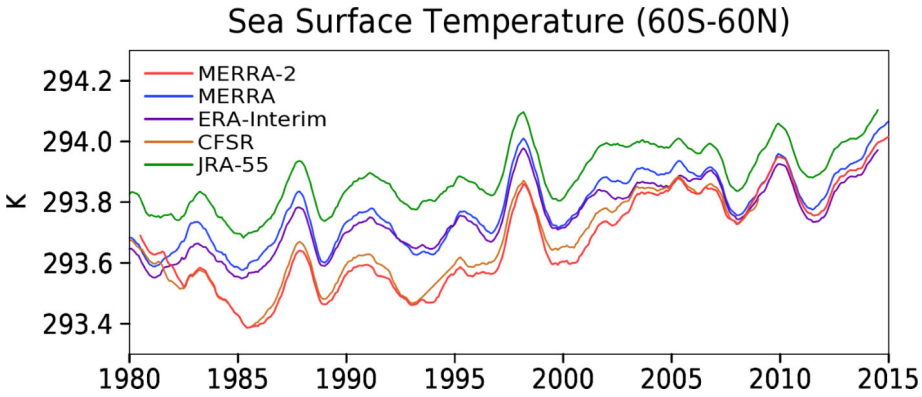

Figure 5:

Time series of 12-month running mean prescribed sea surface temperature for various reanalyses, averaged between 60°N and 60°S. The units are K. Results for MERRA-2 are derived from the data collection described in GMAO (2015f).

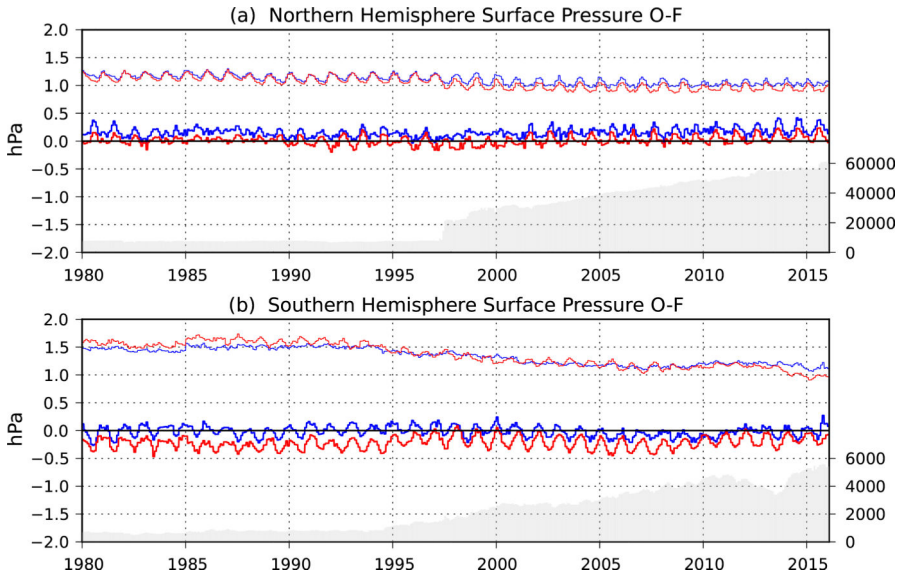

Figure 6:

Monthly mean (thick lines) and RMS (thin lines) background departures for surface pressure observations assimilated in MERRA (blue) and MERRA-2 (red). Results are shown for the (a) Northern Hemisphere and (b) Southern Hemisphere. The units are hPa. Also shown are the corresponding monthly mean counts of surface pressure observations assimilated in MERRA-2 (gray shaded).

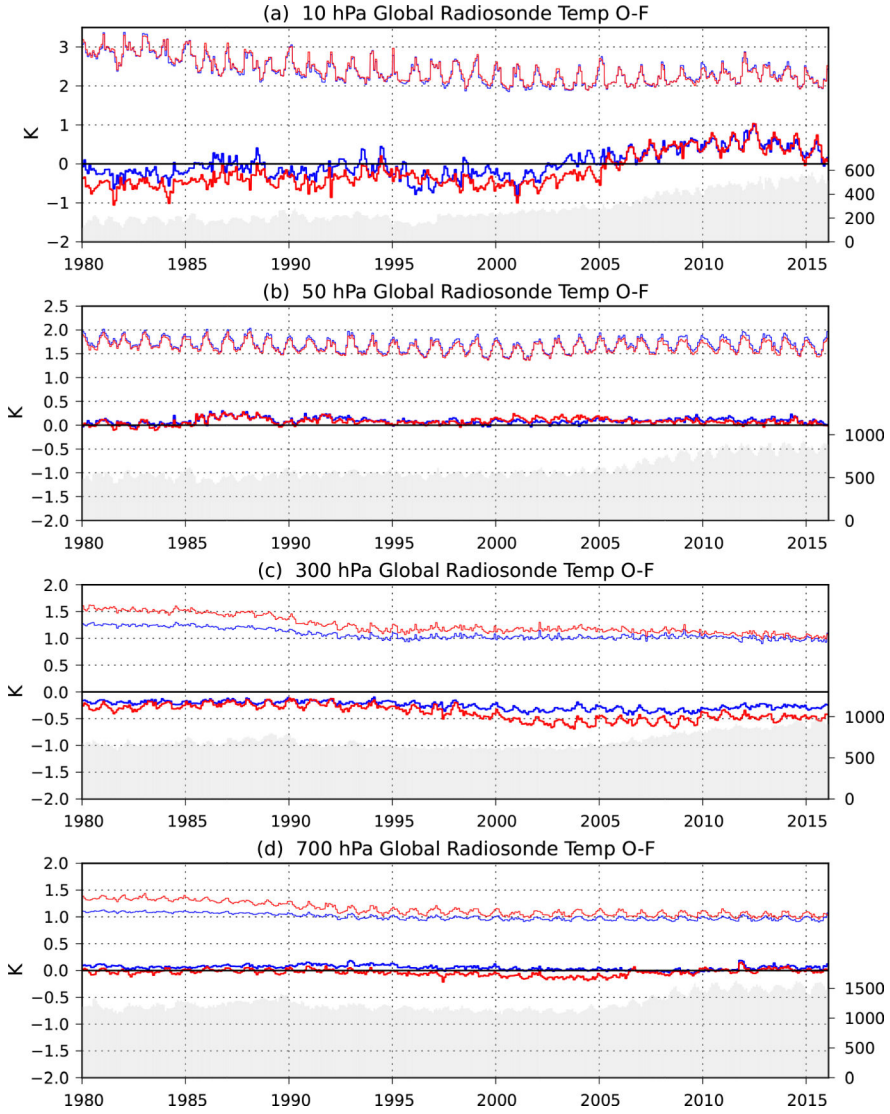

Figure 7:

Global monthly mean (thick lines) and RMS (thin lines) background departures for radiosonde temperature observations assimilated in MERRA (blue) and MERRA-2 (red). Results are shown for the pressure levels (a) 10 hPa, (b) 50 hPa, (c) 300 hPa and (d) 700 hPa. The units are K. Also shown are the corresponding monthly mean counts of radiosonde temperature observations assimilated in MERRA-2 (gray shaded).

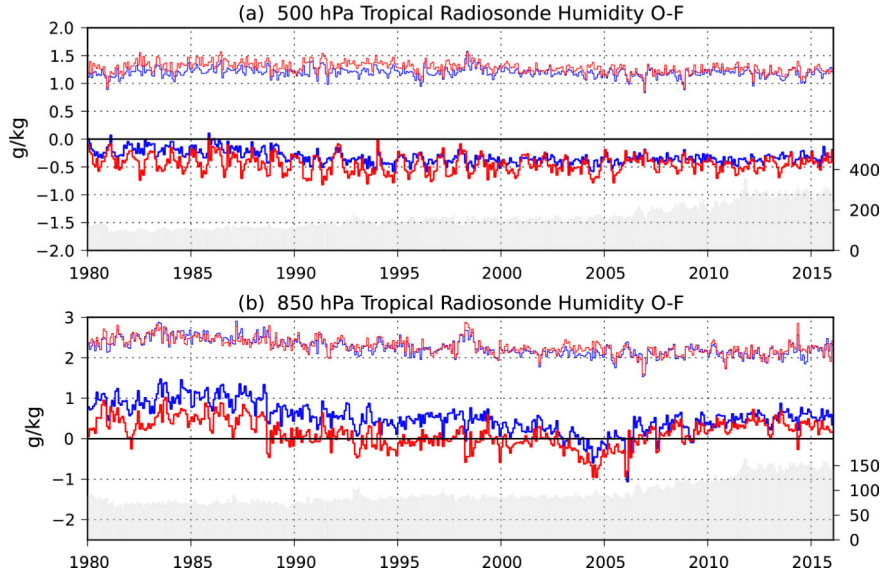

Figure 8:

As in Figure 7, except for radiosonde specific humidity observations in the tropics (20°N-20°S) at (a) 500 hPa and (b) 850 hPa. The units are g kg^{-1}.

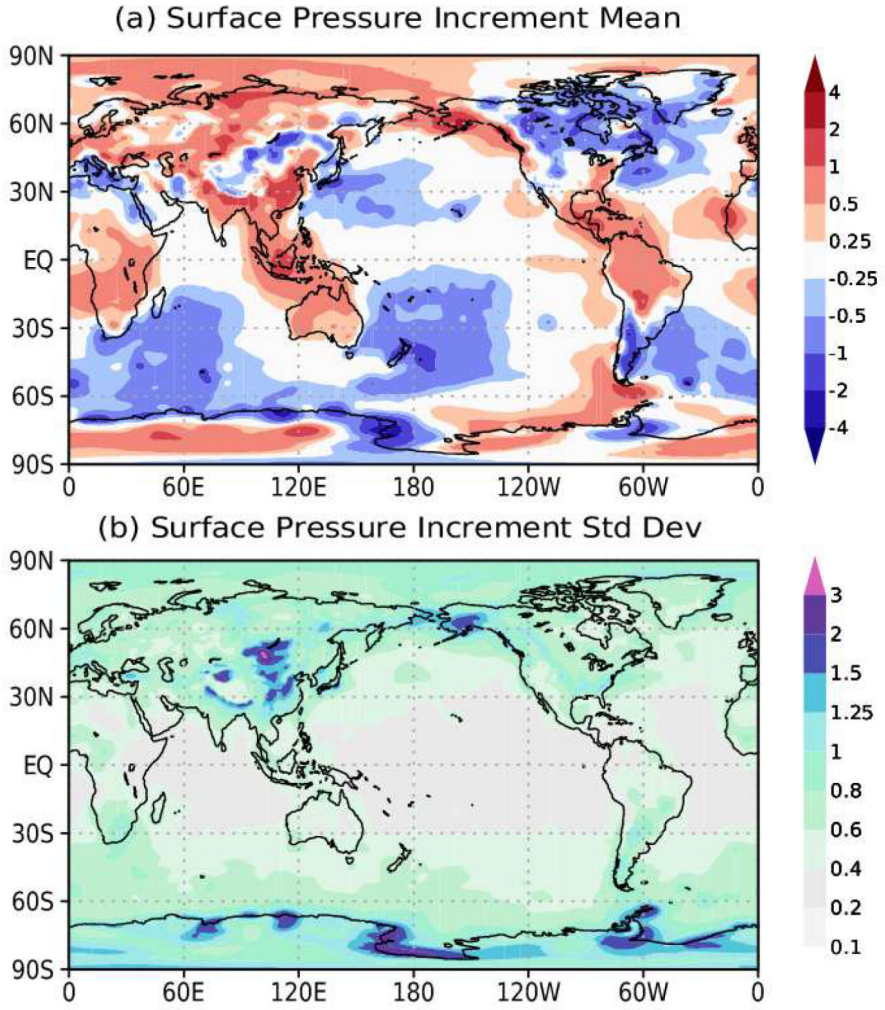

Figure 9:

(a) Mean and (b) standard deviation of the monthly mean analysis tendency of surface pressure for the period January 1980 through December 2015. Monthly mean values are based on four synoptic times daily. The units are hPa day^{-1}. Results are derived from the data collection described in GMAO (2015k).

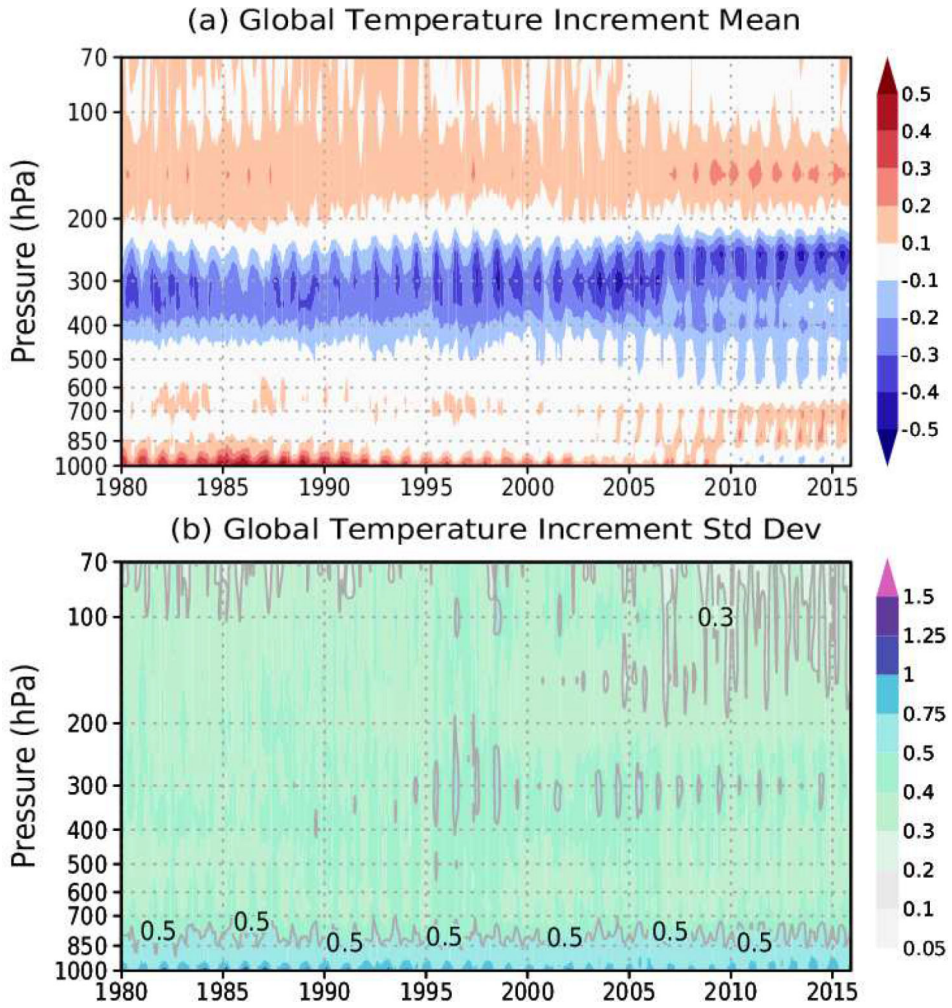

Figure 10:

Global (a) mean and (b) standard deviation of the monthly mean analysis tendency of temperature from 1000 to 70 hPa. Monthly means values are based on four synoptic times daily. The units are K day^{-1}. Results are derived from the data collection described in GMAO (2015n).

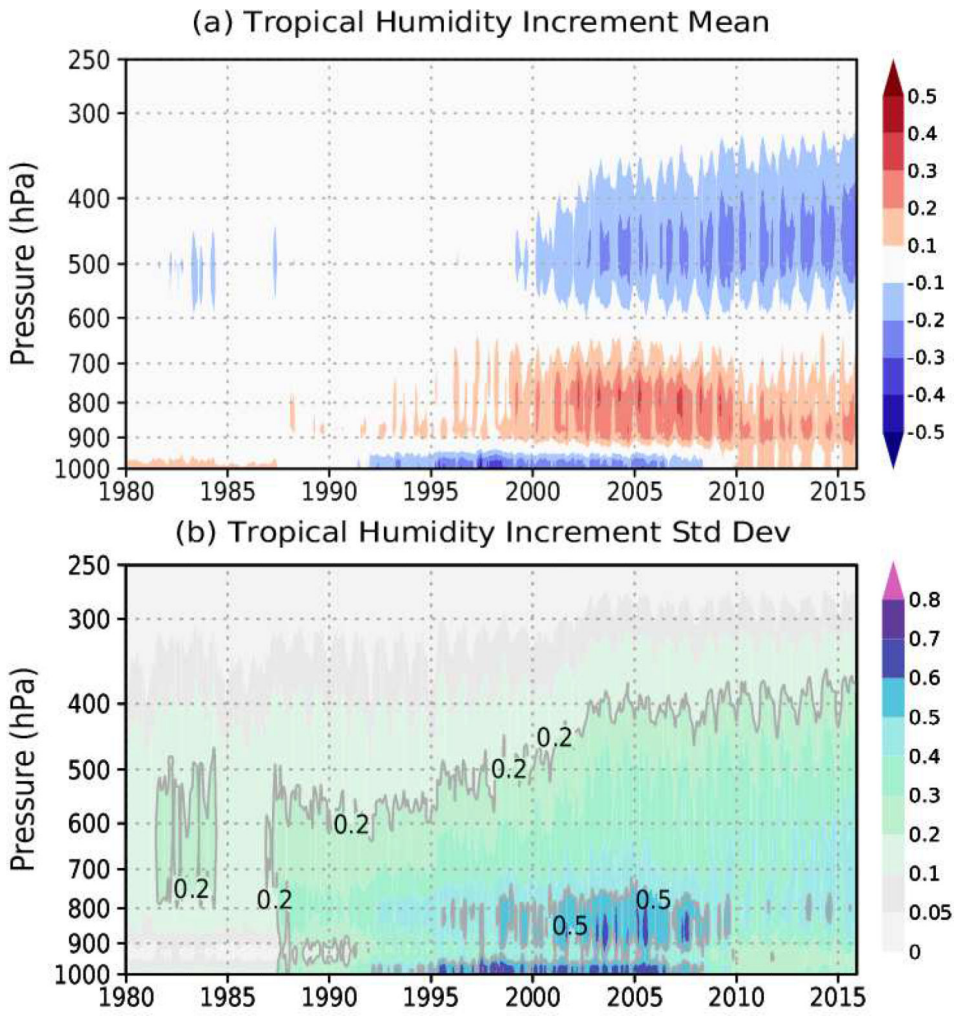

Figure 11:

As in Figure 10, except for specific humidity in the tropics (20°N-20°S) from 1000 to 250 hPa. The units are g kg^{-1} day^{-1}. Results are derived from the data collection described in GMAO (2015l).

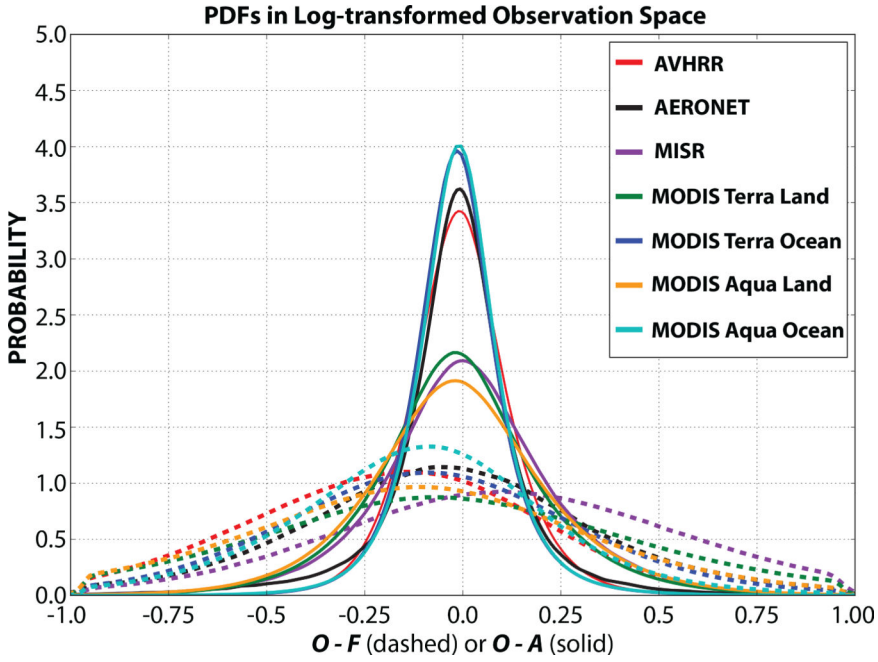

Figure 12:

Probability distribution functions (PDFs) of observation minus forecast (O-F, dashed) and observation minus analysis (O-A, solid) differences in observation space, collocated in space and time for each sensor in the MERRA-2 aerosol observing system. The PDFs are calculated from innovation data in log-transformed space (ln(AOD+0.01)) to ensure distributions are positive and Gaussian. The time periods considered include AVHRR (1993–1999), MODIS Terra (2001–2014), MODIS Aqua (2003–2014), MISR (2001–2012), and AERONET (ANET 2000–2013).

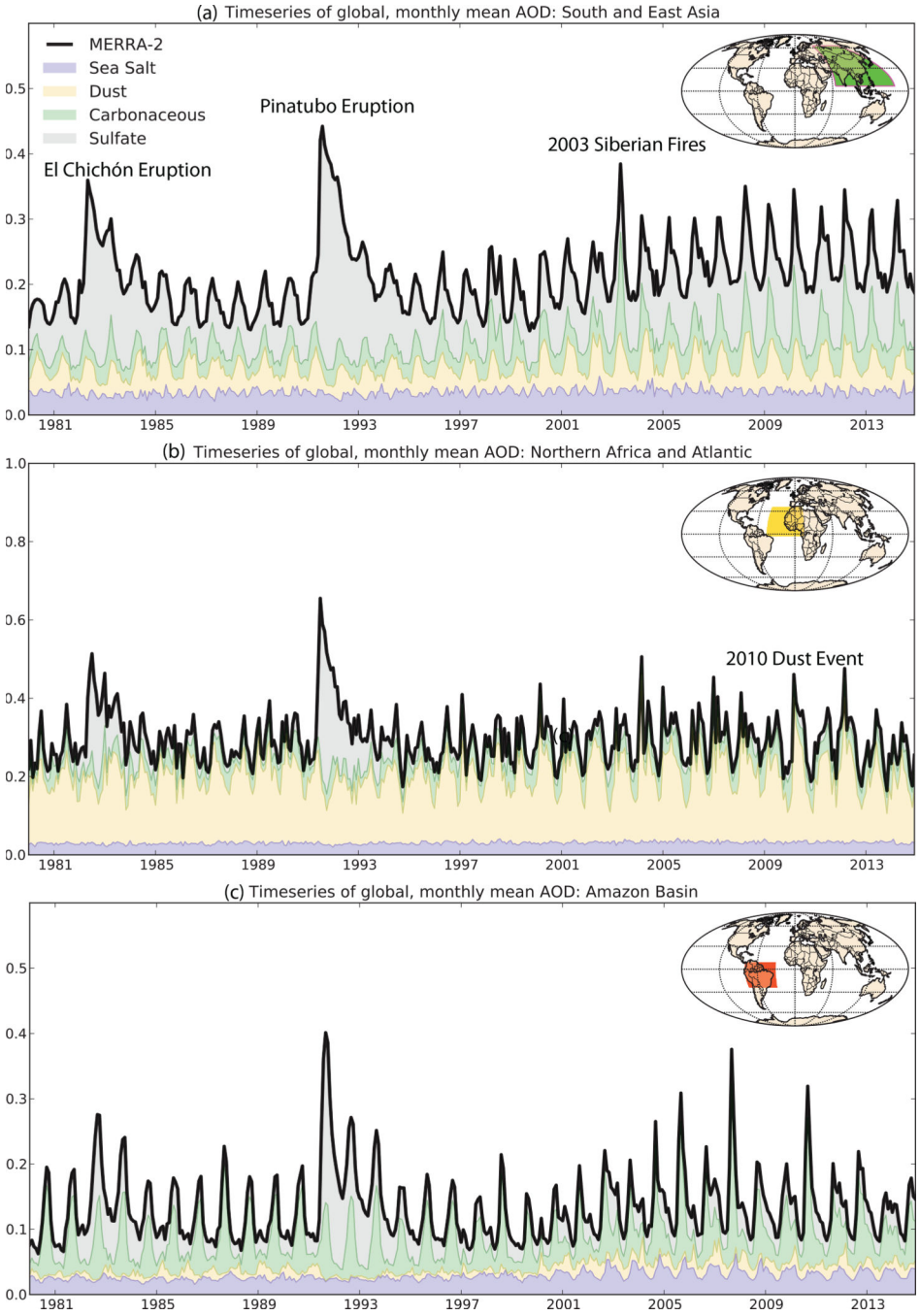

Figure 13:

Time series of area-weighted aerosol optical depth (AOD) from the MERRA-2 aerosol reanalysis averaged over major aerosol source regions: (a) South and East Asia [5°N-55°N, 65°W-160°W], (b) northern Africa [2.5°S-30°N, 45°W-15°E], and (c) the Amazon Basin in South America [20°S-7.5°N, 80°W-30°W]. The total AOD (thick black line) is the sum of contributions from sea salt (blue), dust (yellow), carbonaceous (black and organic carbon, green), and sulfate (grey) AOD. Results are derived from the data collection described in GMAO (2015g).

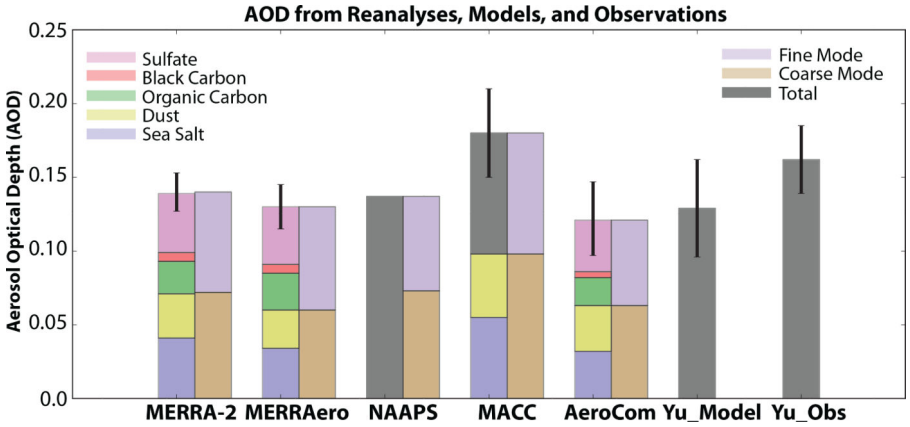

Figure 14:

Aerosol optical depth (AOD) from aerosol reanalyses (MERRA-2, MERRAero, NAAPS, MACC), inter-model comparisons (AeroCom Phase I, Yu_Model), and observations (Yu_Obs) for the period 2003–2010. Where available, total AOD is broken down by component species (left bar) and by fine and coarse mode (right bar). For MERRA-2 and MERRAero, the error bar represents the standard deviation of the monthly-mean AOD for the period 2003–2010. For MACC, the error bar is the uncertainty in the total AOD from Bellouin et al. (2013). AeroCom (Kinne et al., 2006) and Yu et al. (2006) uncertainty are the inter-model or inter-observational standard deviations. Coarse mode is defined as the sum of dust plus sea salt AOD, with the remainder of the AOD assigned to the fine mode. Results for MERRA-2 are derived from the data collection described in GMAO (2015g).

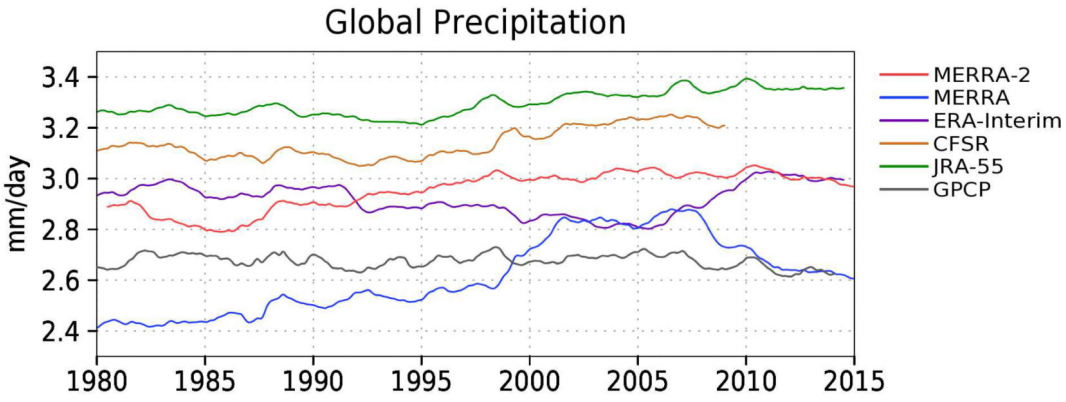

Figure 15:

Time series of 12-month running mean globally averaged precipitation for several reanalyses and the GPCP merged gauge satellite data product. The units are mm day^{-1}. Results for MERRA-2 are derived from the data collection described in GMAO (2015h).

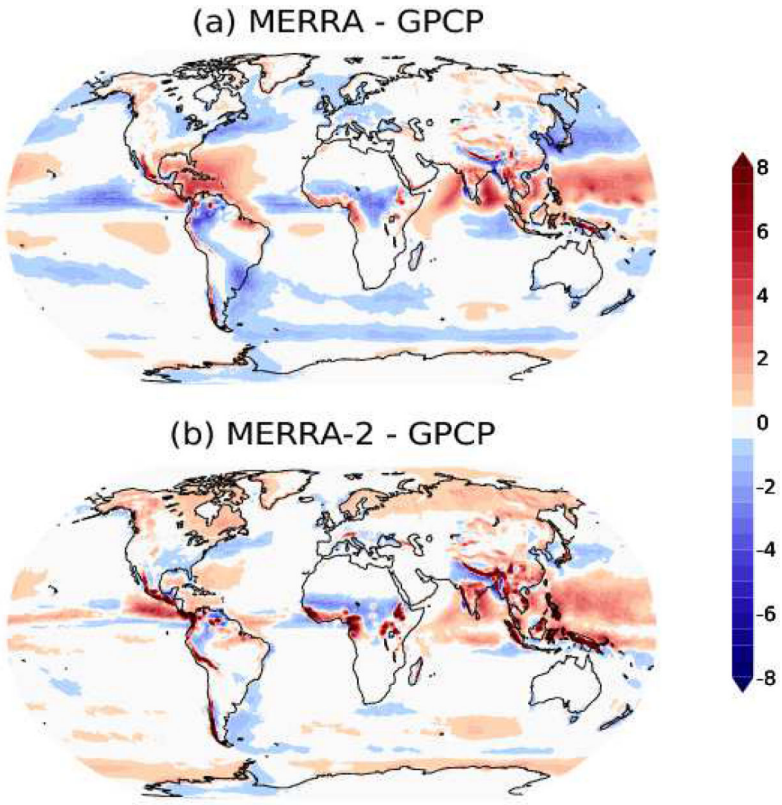

Figure 16:

Time-averaged precipitation differences during June-July-August for (a) MERRA minus GPCP and (b) MERRA-2 minus GPCP for the period 1980–2015. The units are mm day^{-1}. Results for MERRA-2 are derived from the data collection described in GMAO (2015h).

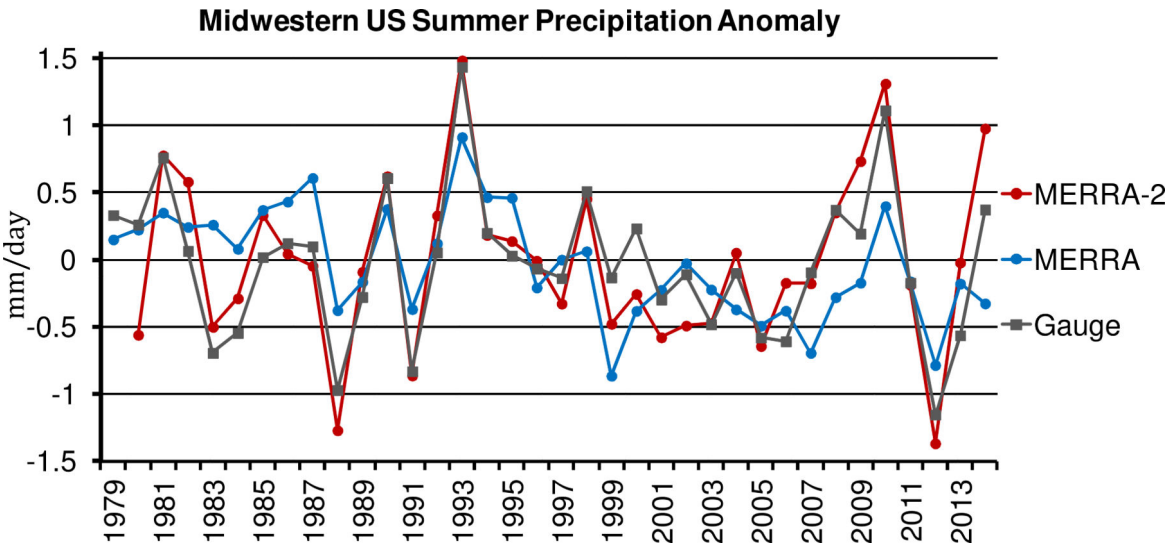

Figure 17:

Time series of midwestern US summer seasonal precipitation anomalies, following Bosilovich (2013). The anomalies are computed from the June-July-August mean for the period 1980–2011. The gauge data are from NOAA/CPC gridded daily data for the US (Xie et al. 2007). The units are mm day^{-1}. Results for MERRA-2 are derived from the data collection described in GMAO (2015h).

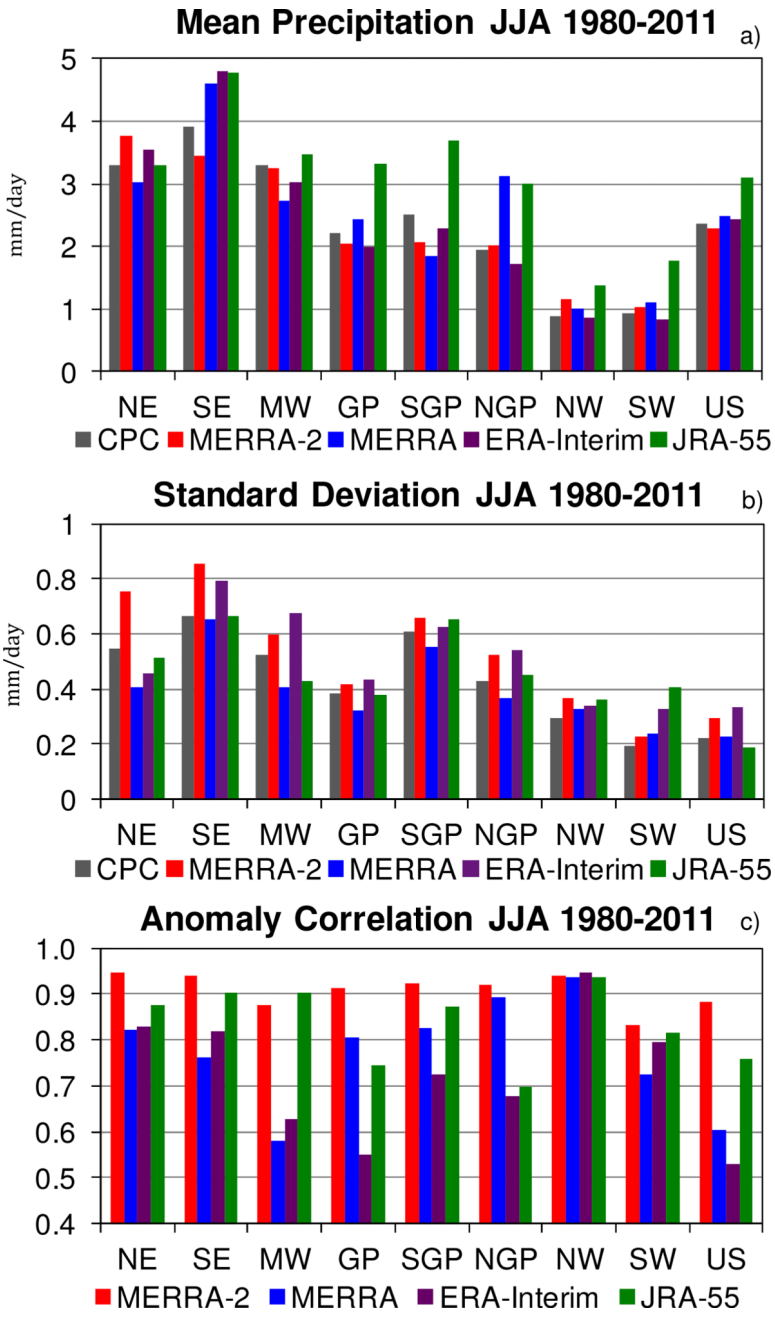

Figure 18:

Regional summary statistics for the US summer seasonal anomaly time series of precipitation: (a) mean (mm day^{-1}), (b) standard deviation (mm day^{-1}), and (c) anomaly correlation to CPC gauge observations. The anomalies are computed from the June-July-August mean for the period 1980–2011. The regions lie within the continental US and are defined as in Bosilovich (2013): Northeast (NE), Southeast (SE), Midwest (MW), Great Plains (GP), Southern Great Plains (SGP), Northern Great Plains (NGP), Northwest (NW), Southwest (SW), and the accumulation of all area in these regions (US). Results for MERRA-2 are derived from the data collection described in GMAO (2015h).

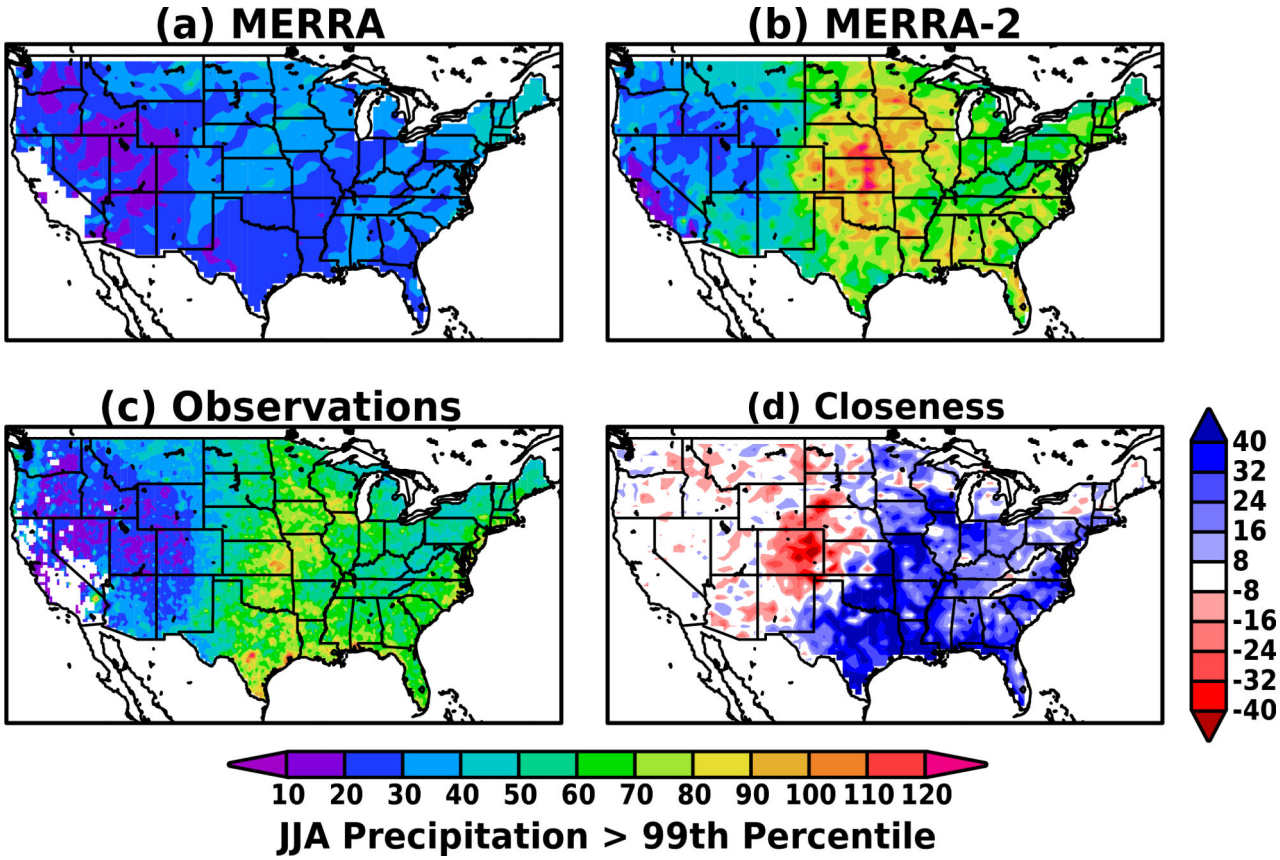

Figure 19:

Average amount of precipitation that exceeds the 99th percentile during June-July-August for the period 1980–2013 for (a) MERRA, (b) MERRA-2, and (c) CPC gauge observations. Panel (d) shows the closeness of each reanalysis to the CPC observations for the same period, defined as |MERRA-2 − CPC| − |MERRA − CPC|, where the vertical bars indicate absolute differences and the names indicate the set of time-averaged grid-point values for each data type. In (d), blue (red) shades indicate that MERRA-2 (MERRA) is closer to the CPC observations. The units in all panels are mm day^{-1}. Results for MERRA-2 are derived from the data collection described in GMAO (2015d).

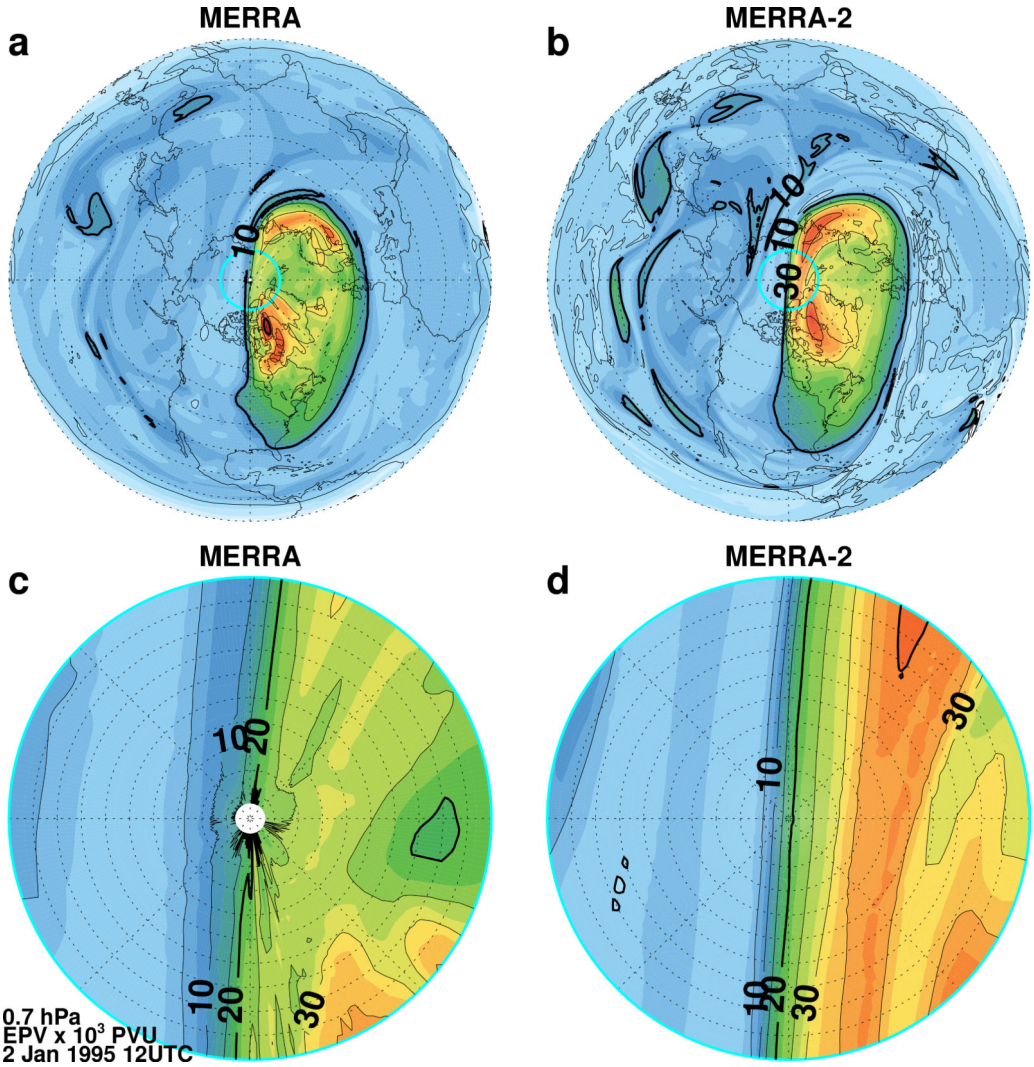

Figure 20:

Ertel's potential vorticiity (EPV, $\times 10^3$ potential vorticity units, PVU; 1 PVU = $10^{-6}m^{-2}s^{-1}K\ kg^{-1}$) at 0.7 hPa on 2 January 1995 12 UTC for (a) MERRA and (b) MERRA-2 for the Northern Hemisphere. Polar cap detail (80°−90°N) for (c) MERRA and (d) MERRA-2. Color shading interval is 2.5×10^3 PVU. Black contour interval is 10×10^3 PVU in (a) and (b) and 5×10^3 PVU in (c) and (d). Cyan circle denotes 80°N latitude. Results are derived from the data collection described in GMAO (2015c).

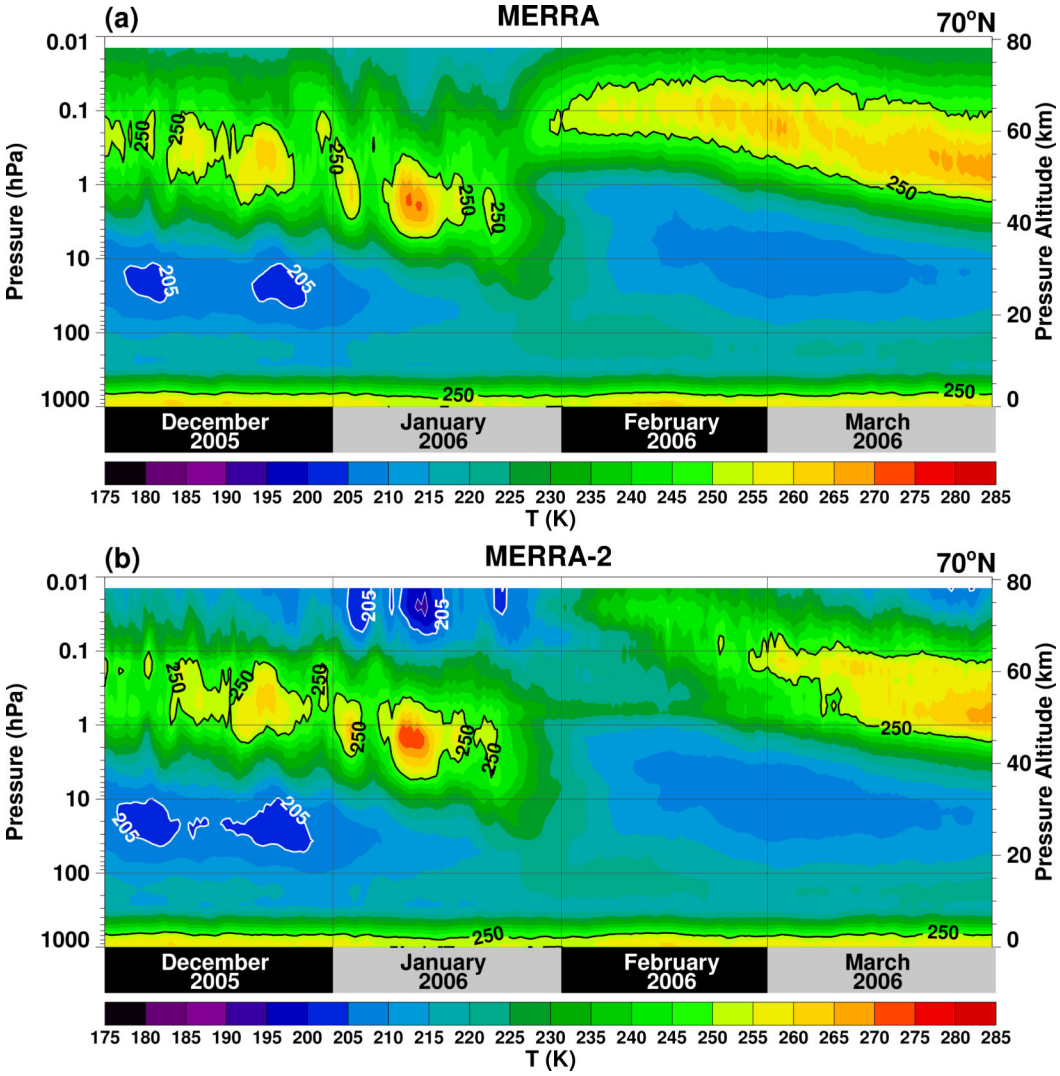

Figure 21:

Time-altitude section of zonally averaged temperature at 70°N for (a) MERRA and (b) MERRA-2. The time resolution is twice daily (00 and 12 UTC) for December 2005-March 2006. The contour interval is 5 K.

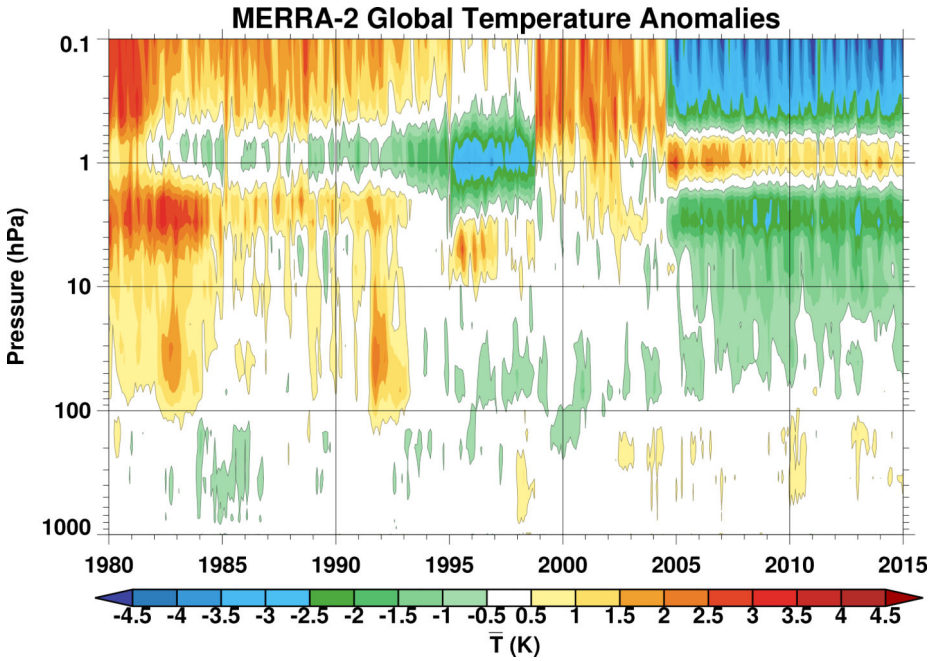

Figure 22:

Monthly and globally averaged temperature anomaly for MERRA-2 as a function of time. The annual cycle and mean for 1980–2015 have been removed. The MLS temperatures were introduced at levels above 5 hPa beginning in August 2004. Results are derived from the data collection described in GMAO (2015c).

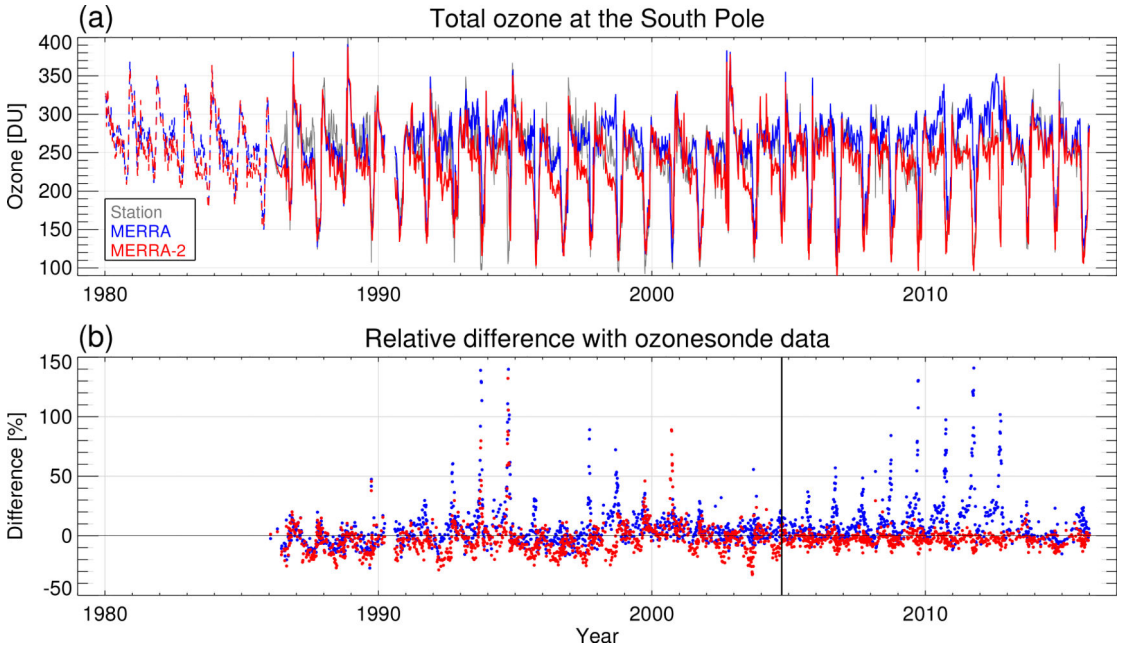

Figure 23:

Time series of (a) total ozone (Dobson units, DU) at the South Pole derived from individual ozonesonde measurements (gray) and from collocated values in MERRA (blue) and MERRA-2 (red). Note that ozonesonde measurements are unavailable prior to 1986; see text for details. The reanalysis-minus-ozonesonde differences divided by sonde total ozone are shown in (b) for MERRA (blue) and MERRA-2 (red). The black vertical line in (b) separates the SBUV and Aura periods. (Figure from Wargan et al. 2016.) Results for MERRA-2 are derived from the data collection described in GMAO (2015a).

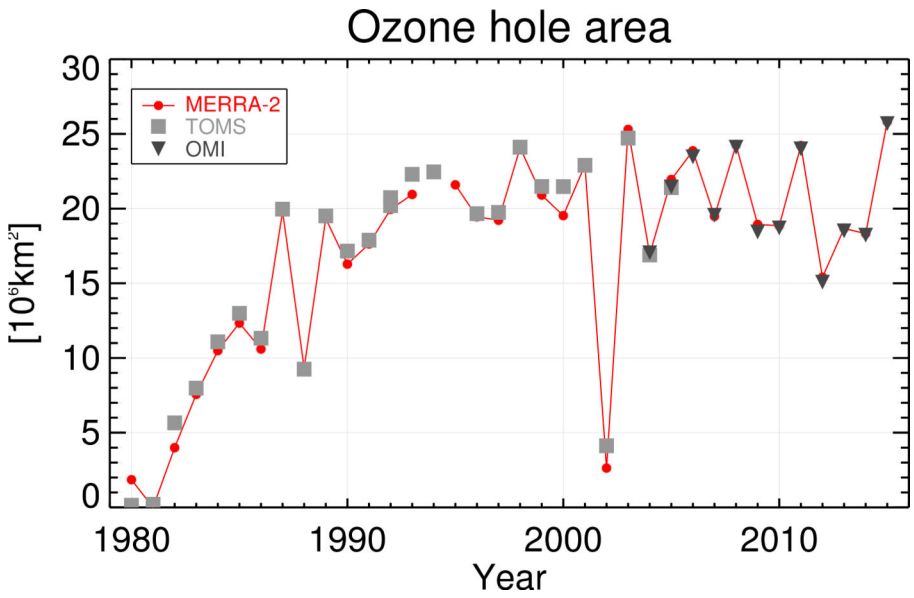

Figure 24:

Time series of the Antarctic ozone hole area calculated from MERRA-2 ozone fields averaged between 20 September and 10 October for the years 1980–2015 (red curve with circles). Also shown are values derived from TOMS (gray squares) and OMI (black triangles) observations. The units are 10^6 km^2. Results for MERRA-2 in 1994 are excluded due to insufficient SBUV data coverage in the Southern Hemisphere, which significantly degraded the analysis; see text for details. Results for MERRA-2 are derived from the data collection described in GMAO (2015a).

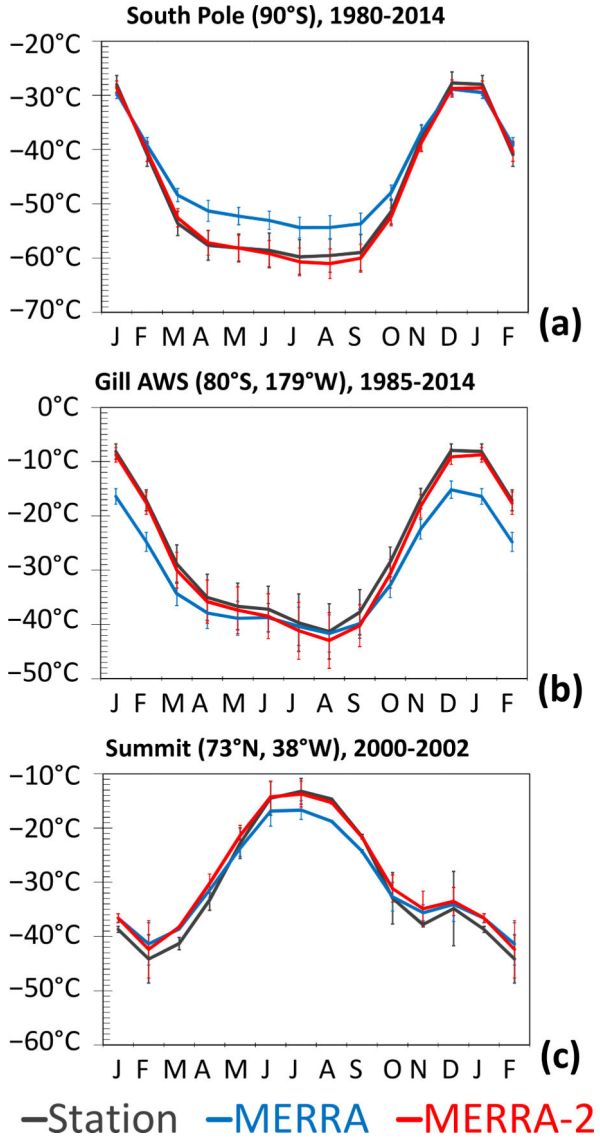

Figure 25:

Average annual cycle of 2-m air temperature in MERRA and MERRA-2 at (a) South Pole station (90°S; 1980–2014; Turner et al., 2004), (b) Gill automatic weather station (80°S, 179°W; 1985–2014; Turner et al., 2004), and (c) Summit, Greenland (73°N, 38°W; 2000–2002; Hoch, 2005). The units are °C. Vertical bars denote ±1 standard deviation of the multi-year time series for each month. Results for MERRA-2 are derived from the data collections described in GMAO (2015i, j, m).

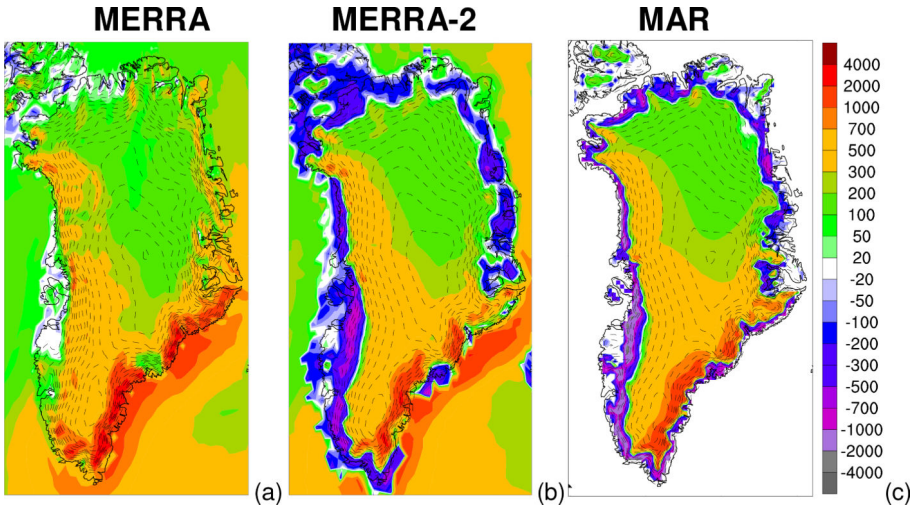

Figure 26:

Surface mass balance for the Greenland Ice Sheet for the period 1980–2012 in (a) MERRA, (b) MERRA-2, and (c) MAR regional climate model (Fettweis 2007). The units are mm yr^{-1} water-equivalent. Surface topography (including ice sheet) is contoured with dashed lines every 200 m. Results for MERRA-2 are derived from the data collections described in GMAO (2015i, j, m).

Table 1:

Observation types assimilated in MERRA-2, including their usage datesand sources. Bold fonts indicate observation types not assimilated in MERRA. Acronyms are defined in the Appendix.

Data Type	MERRA-2 Dates	Source
	Conventional	
Raob, Pibal, Dropsonde	1 Jan 1980-present	See Rienecker et al. (2011)
AIREP, PIREP, ASDAR, MDCRS aircraft	1 Jan 1980-present	NCEP, ECMWF, JMA
PAOB	1 Jan 1980–17 Aug 2010	BOM
Surface land	1 Jan 1980-present	NCEP
Surface ship and buoy	1 Jan 1980-present	ICOADS
	Ground-Based Remotely Sensed	
Wind profiler	14 May 1992-present	UCAR, NCEP
NEXRAD VAD wind	16 June 1997-present	NCEP
	Satellite-Derived Wind	
GMS, MTSAT, Himawari atmos. motion vector	1 Jan 1980-present	NCEP, JMA
Meteosat atmos. motion vector	1 Jan 1980-present	NCEP, EUMETSAT
GOES atmos. motion vector	1 Jan 1980-present	NCEP
AVHRR atmos. motion vector	**1 Oct 1982—present**	**CIMSS**
SSM/I surface wind speed	9 Jul 1987–4 Nov 2009	RSS
ERS-1 surface wind vector	5 Aug 1991–21 May 1996	ESA
ERS-2 surface wind vector	19 Mar 1996–29 Mar 2011	ESA
QuikSCAT surface wind vector	19 Jul 1999–22 Nov 2009	JPL
MODIS atmos. motion vector	2 Jul 2002-present	CIMSS, NCEP
SSMIS surface wind speed	**23 Oct 2003–29 Oct 2013**	**RSS**
WindSat surface wind vector	**13 Aug 2007–4 Aug 2012**	**NCEP**
ASCAT surface wind vector	**15 Sep 2008 present**	**NCEP**
	Satellite-Retrieved	
SBUV, SBUV/2 ozone	1 Jan 1980–31 Sep 2004	NASA/GES DISC
SSM/I rain rate	9 Jul 1987–16 Sep 2009	NASA/GES DISC
TMI rain rate	1 Jan 1998–8 Apr 2015	NASA/GES DISC
MLS temperature	**13 Aug 2004-present**	**NASA/GES DISC**
MLS ozone	**1 Oct 2004-present**	**NASA/GES DISC**
OMI total column ozone	**1 Oct 2004 present**	**NASA/GES DISC**
	Radio Occultation	
GPSRO bending angle	**14 July 2004 present**	**NCAR, NCEP**
	Satellite Radiance	
TOVS	1 Jan 1980–10 Oct 2006	NCAR, NESDIS

Data Type	MERRA-2 Dates	Source
SSM/I	9 Jul 1987–4 Nov 2009	RSS
ATOVS (NOAA-15, -16, -17, -18)	21 Jul 1998-present	NESDIS
GOES (G08, G10, G11, G12 Low Res.)	24 April 2001–31 March 2007	NCEP, NESDIS
AMSU-A (Aqua)	1 Sep 2002-present	NASA/GES DISC
AIRS	1 Sep 2002-present	NASA/GES DISC
GOES (G11, G12, G13, G15 Full Res.)	**1 April 2007-present**	**NESDIS**
ATOVS (NOAA-19, Metop-A, -B)	**21 May 2007-present**	**NESDIS**
IASI	**17 Sep 2008-present**	**NESDIS**
ATMS	**16 Nov 2011-present**	**NESDIS**
SEVIRI	**15 Feb 2012-present**	**NESDIS**
CrIS	**7 Apr 2012-present**	**NESDIS**

Table 2:

Nominal channel selections for satellite radiances assimilated in MERRA-2. Usage can vary for individual satellite platforms as a result of sensor failure or quality control decisions.

Sensor	Assimilated Channels
MSU	2–4
AMSU-A	4–14
ATMS	5–15, 17–22
AMSU-B	1–5
MHS	1–5
SSM/I	1–7
SSU	1–3
HIRS	2–8, 10–12
AIRS	See McCarty et al. 2016
IASI	See McCarty et al. 2016
CrIS	See McCarty et al. 2016
GOES Sounder	1–8, 10–12
SEVIRI	2,3

Table 3:

Sea surface temperature and sea ice concentration data products used in MERRA-2.

MERRA-2 dates	SST and SIC product
1 January 1980 – 31 December 1981	CMIP mid-monthly 1°
1 January 1982 – 31 December 2002	NOAA OISST daily 1/4° (AVHRR)
1 January 2003 – 31 March 2006	NOAA OISST daily 1/4° (AVHRR, AMSR-E)
1 April 2006 - present	OSTIA daily 1/20°

Table 4:

Clear-sky Direct Radiative Effect (DRE) from Reanalyses and Observations

	Yu et al. (2006) Obs.[a]	Yu et al. (2006) Models[b]	MERRA-2[c]	MERRAero[c]	MACC[d]
			Land-area Average		
AOD	0.225 ± 0.038	0.178 ± 0.029	**0.180** ± 0.027	0.171 ± 0.030	0.203 ± 0.030
AAOD	-	-	**0.012** ± 0.002	0.016 ± 0.003	0.010 ± 0.003
TOA DRE	−4.85 ± 0.45	−2.80 ± 1.19	**−3.09** ± 0.62	−3.11 ± 0.70	−6.40 ± 1.00
SFC DRE	−11.70 ±1.20	−7.20 ± 1.86	**−8.35** ± 1.82	−8.64 ± 2.04	−11.50 ± 1.90
ATM DRE	6.85 ± 0.75	4.90 ± 0.81	**5.26** ± 1.23	5.53 ± 1.37	5.10
			Ocean-area Average		
AOD	0.138 ± 0.024	0.100 ± 0.042	**0.123** ± 0.008	0.111 ± 0.010	0.170 ± 0.030
AAOD	-	-	**0.005** ± 0.001	0.005 ± 0.001	0.007 ± 0.001
TOA DRE	−5.45 ± 0.70	−3.50 ± 1.28	**−3.65** ± 0.21	−3.44 ± 0.24	−7.70 ± 1.50
SFC DRE	−8.80 ± 1.65	−4.80 ± 1.60	**−5.74** ± 0.41	−5.58 ± 0.47	−10.60 ± 1.90
ATM DRE	3.60 ± 1.30	1.30 ± 0.72	**2.09** ± 0.27	2.14 ± 0.29	2.90

[a] Median and standard deviation from satellite-derived estimates in Yu et al. (2006).

[b] Median and standard deviation from 4 global models in Yu et al. (2006).

[c] Climatological global area-weighted average (± monthly standard deviation) for Y2003-Y2010.

[d] For MACC, the Y2003-Y2010 global mean and uncertainty is given following Bellouin et al. (2013).